1   Complex refractive indices and single scattering albedo of global dust
2   aerosols in the shortwave spectrum and relationship to iron content and size

3   Claudia Di Biagio[1], Paola Formenti[1], Yves Balkanski[2], Lorenzo Caponi[1,3], Mathieu Cazaunau[1],
4   Edouard Pangui[1], Emilie Journet[1], Sophie Nowak[4], Meinrat O. Andreae[5,6], Konrad Kandler[7], Thuraya
5   Saeed[8], Stuart Piketh[9], David Seibert[10], Earle Williams[11], and Jean-Francois Doussin[1]

6   [1] *Laboratoire Interuniversitaire des Systèmes Atmosphériques (LISA), UMR7583, CNRS, Université*
7   *Paris Est Créteil et Université Paris Diderot, Institut Pierre et Simon Laplace, Créteil, France*
8   [2] *Laboratoire des Sciences du Climat et de l'Environnement, CEA CNRS UVSQ, 91191, Gif sur Yvette,*
9   *France*
10   [3] *PM_TEN srl, Piazza della Vittoria 7/14, 16121, Genoa, Italy*
11   [4] *Plateforme RX UFR de chimie, Université Paris Diderot, Paris, France*
12   [5] *Biogeochemistry Department, Max Planck Institute for Chemistry, P.O. box 3060, 55020, Mainz, Ger-*
13   *many*
14   [6] *Geology and Geophysics Department, King Saud University, Riyadh, Saudi Arabia*
15   [7] *Institut für Angewandte Geowissenschaften, Technische Universität Darmstadt, Schnittspahnstr. 9,*
16   *64287 Darmstadt, Germany*
17   [8] *Science department, College of Basic Education, Public Authority for Applied Education and Training,*
18   *Al-Ardeya, Kuwait*
19   [9] *Climatology Research Group, Unit for Environmental Science and Management, North-West Univer-*
20   *sity, Potchefstroom, South Africa*
21   [10] *Walden University, Minneapolis, Minnesota, USA*
22   [11] *Parsons Laboratory, Massachusetts Institute of Technology, Cambridge, Massachusetts, USA*
23
24   Correspondence to: C. Di Biagio (claudia.dibiagio@lisa.u-pec.fr)
25

27   **Abstract**

28   The optical properties of airborne mineral dust depend on its mineralogy, size distribution, shape, and

29   might vary between different source regions. To date, large differences in refractive index values found

30   in the literature have not been fully explained. In this paper we present a new dataset of complex re-

31   fractive indices ($m=n–ik$) and single scattering albedos (SSA) for 19 mineral dust aerosols over the 370–

32   950 nm range in dry conditions. Dust aerosols were generated from natural parent soils from eight

33   source regions (Northern Africa, Sahel, Middle East, Eastern Asia, North and South America, Southern

34   Africa, and Australia). These were selected to represent the global scale variability of the dust mineral-

35   ogy. Dust was re–suspended into a 4.2 m^3 smog chamber where its spectral shortwave scattering (β_{sca})

36   and absorption (β_{abs}) coefficients, number size distribution, and bulk composition were measured. The

37   complex refractive index was estimated by Mie calculations combining optical and size data, while the

38   spectral SSA was directly retrieved from β_{sca} and β_{abs} measurements. Our results show that the imagi-

39   nary part of the refractive index (k) and the SSA largely vary from sample to sample, with values for k

40   in the range 0.001 to 0.009 at 370 nm and 0.0003 to 0.002 at 950 nm, and values for SSA in the range

41   0.70 to 0.96 at 370 nm and 0.95 to 0.99 at 950 nm. In contrast, the real part of the refractive index (n)

42   is mostly source (and wavelength) independent, with an average value between 1.48 and 1.55. The

43   sample–to–sample variability in our dataset of k and SSA is mostly related to differences in the dust's

44   iron content. In particular, a wavelength–dependent linear relationship is found between the magnitude

45   of k and SSA and the mass concentrations of both iron oxide and total elemental iron. As an intrinsic

46 property of matter, k is independent of size. When the iron oxide content exceeds >3%, the SSA linearly

47 decreases with increasing fraction of coarse particles at short wavelengths (< 600 nm).

48 We recommend that source–dependent values of the SW spectral refractive index and SSA are used

49 in models and remote sensing retrievals instead of generic values. In particular, the close relationships

50 found between k/SSA and the iron content in dust enable establishing predictive rules for spectrally–

51 resolved SW absorption based on particle composition.

52

53 **Introduction**

54 With teragrams of annual emissions, a residence time of about 1–2 weeks in the atmosphere, and a

55 planetary–scale transport, mineral dust aerosols are a global phenomenon (Uno et al., 2009; Ginoux et

56 al., 2012), and contribute significantly to the global and regional aerosol loading (Ridley et al., 2016)

57 and direct radiative effect (Miller et al., 2014).

58 However, large uncertainties still persist on the magnitude and overall sign of the dust direct radiative

59 effect (Boucher et al., 2013; Highwood and Ryder, 2014; Kok et al., 2017). One of the major sources of

60 this uncertainty is our insufficient knowledge of the dust's absorption properties in the shortwave (SW)

61 and longwave (LW) spectral ranges (e.g., Balkanski et al., 2007; Samset et al., 2018), given that mineral

62 dust contains large particles and a variety of minerals absorbing over both spectral regions (e.g. iron

63 oxides, clays, quartz and calcium–rich species, Sokolik and Toon, 1999; Lafon et al., 2006; Di Biagio

64 et al., 2014a, b). Global and regional scale mapping of dust absorption remains limited and more infor-

65 mation is required (Samset et al., 2018).

66 Aerosol absorption is represented both by the imaginary part (k) of the complex refractive index (m=n–

67 ik) of its constituent material, and by the single scattering albedo (SSA, i.e., the ratio of the scattering

68 to extinction coefficient) of the particle population, as well as by the mass absorption efficiency (MAE,

69 units of $m^2\ g^{-1}$), i.e., the absorption coefficient per unit of aerosol mass concentration.

70 In the shortwave spectral range, absorption by dust accounts for up to ~10–20% of its total extinction.

71 Dust absorption is highest in the UV–VIS, and almost nil towards the near IR (Cattrall et al., 2003;

72 Redmond et al., 2010), due to the combined contribution of large particles in the size distribution and

73 the dust's mineralogy, notably the presence of iron oxides (Karickhoff and Bailey, 1973; Lafon et al.,

74 2006; Derimian et al., 2008; Moosmüller et al., 2012; Formenti et al., 2014a; 2014b; Engelbrecht et al.,

75 2016; Caponi et al., 2017). The mineralogy of mineral dust varies according to that of the parent soils

76 (Nickovic et al., 2012; Journet et al., 2014). Consequently, dust aerosols of different origins should be

77 more or less absorbing in the SW, and have different imaginary spectral refractive index and SSA. Field

78 and laboratory measurements, including ground–based and spaceborne remote sensing, show that k

79 varies at a regional scale by almost two orders of magnitude (0.0001–0.008 at 550 nm) with corre-

80 sponding SSAs between 0.80 and 0.99 at 550 nm (Volz 1972; Patterson et al., 1977; Shettle and Fenn,

81 1979; Dubovik et al., 2002; Haywood et al., 2003; Sinyuk et al., 2003; Linke et al., 2006; Osborne et al.,

82 2008; Müller et al., 2009; Otto et al., 2009; Petzold et al., 2009; Schladitz et al., 2009; McConnell et al.,

83 2010; Formenti et al., 2011; Wagner et al., 2012; Ryder et al., 2013a; Engelbrecht et al., 2016; Rocha-

84   Lima et al., 2018). Albeit some variability being instrumental or analytical (differences in the sampled

85   size fraction or in the method used to retrieve optical parameters), differences persist when the same

86   measurement approach and retrieval method are applied, e.g., in AERONET inversions, supporting the

87   dependence of dust k and SSA with location (Dubovik et al., 2002; Koven and Fung, 2006; Su and

88   Toon, 2011). In contrast, the real part (n) of the dust refractive index, mostly related to particle scatter-

89   ing, is estimated to be less variable than the imaginary part, with values between 1.47–1.56 at 550 nm

90   (i.e., Volz, 1972; Patterson et al., 1977; Balkanski et al., 2007; Petzold et al., 2009).

91   Differences in k or SSA caused by the spatial variability of the iron content may affect the sign of the

92   dust radiative effect (heating vs cooling) (Liao and Seinfeld, 1998; Claquin et al. 1999; Miller et al.,

93   2014), and its global and regional implications (Myhre and Stordal, 2001; Colarco et al., 2014; Das et

94   al., 2015; Jin et al., 2016; Bangalath and Stenchikov, 2016; Strong et al., 2018). For instance, various

95   studies suggest that the direct radiative effect of dust has a strong impact on the Western African Mon-

96   soon (Yoshioka et al., 2007; Konaré et al., 2008) and the Indian Summer Monsoon (Vinoj et al., 2014;

97   Das et al., 2015; Jin et al., 2016). However, there is no consensus whether dust increases or decreases

98   precipitation over these regions (Solmon et al., 2008; Jin et al., 2016; Strong et al., 2018). As an exam-

99   ple, Solmon et al. (2008) indicate that dust reduces precipitation over most of the Sahelian region, but

100   increases it over the Northern Sahel–Southern Sahara. This pattern is, however, very sensitive to the

101   dust absorbing properties, and a decrease of few percent in dust absorption may even cancel out the

102   increase of precipitation over the Sahel. Similarly, Jin et al. (2016) show that by varying k from zero to

103   0.008 at 600 nm (i.e., the highest value currently used in models) the dust effect on the Indian Summer

104   Monsoon may shift from negative (reduction of precipitation) to positive (increase of precipitation) val-

105   ues.

106   In spite of this sensitivity, present climate models adopt a globally–constant spectral complex refractive

107   index (and SSA) for dust, and hence still implicitly assume the same dust mineralogical composition at

108   the global scale. Reference values for the refractive index are usually taken from Volz (1972), Patterson

109   et al. (1977), D'Almeida et al. (1991), Shettle and Fenn (1979), Sokolik et al. (1993), Sinyuk et al. (2003),

110   or OPAC (Hess et al., 1998; Koepke et al., 2015). A parameterization of the spectrally–resolved dust

111   refractive index as a function of the mineralogical composition of the particles is desirable to replace

112   the globally constant values in current climate models, in particular for those models that started to

113   incorporate the representation of dust mineralogy into their schemes (Scanza et al., 2015; Perlwitz et

114   al., 2015a, 2015b).

115   Improving our knowledge of the spectral SW refractive index of mineral dust and its relation to particle

116   composition and origin is also key for the detection of dust aerosols in the atmosphere and the quanti-

117   fication of its mass loading, and total and absorption spectral optical depth from active and passive

118   remote sensing (e.g., Ridley et al., 2016). As an example, the retrieval of the dust SSA and optical depth

119   over bright desert surfaces with the MODIS (Moderate Imaging Resolution Spectroradiometer) Deep

120   Blue algorithm (Hsu et al., 2004) applies the Critical Surface Reflectance Method (Kaufman, 1987) to

121   retrieve dust properties from measured Top of Atmosphere (TOA) spectral reflectance. This algorithm

122   depends critically on a priori information on the spectral refractive index (Kaufman et al., 2001; Yoshida

123 et al., 2013). Similarly, active remote sensing techniques (lidar, light detection and ranging) require the

124 knowledge of the extinction-to-backscatter ratio (the lidar ratio), which is also a strong function of the

125 complex index of refraction or SSA of the aerosol particles (e.g., Gasteiger et al., 2011; Shin et al.,

126 2018). Gasteiger et al. (2011) have shown in fact that a 5% change in the SSA at 532 nm can modify

127 by up to 20% the lidar ratio of dust, which means a 20% change in the estimated profile of the dust

128 extinction coefficient and retrieved optical depth from lidar measurements.

129 In this paper we address these issues by reporting the results of a new laboratory investigation of the

130 shortwave refractive index and SSA of dust from various source regions worldwide, in the framework

131 of the RED–DUST project (Di Biagio et al., 2017a; hereafter DB17; Caponi et al., 2017; hereafter C17).

132 Dust optical properties at discrete wavelengths between 370 and 950 nm are derived in conjunction

133 with the particle elemental and mineralogical composition, including total elemental iron and iron oxides.

134 We investigate the relationship of k and SSA to the iron content to provide a parameterization of the

135 dust absorption as a function of its mineralogy, which can be applied to climate models. The depend-

136 ence of dust absorption on the particle coarse size fraction is also investigated to evaluate the change

137 of dust absorption with atmospheric transport time.

138 **2. Experimental set–up and instrumentation**

139 All experiments discussed here and previously described in DB17 and C17 were conducted in the

140 4.2 m^3 stainless–steel CESAM chamber (French acronym for Experimental Multiphasic Atmospheric

141 Simulation Chamber) (Wang et al., 2011). Mineral dust aerosols were generated by mechanical shaking

142 of parent soils using about 15 g of soil sample (first sieved to <1000 μm and then dried at 100 °C)

143 placed in a 1 L Büchner flask and shaken for about 30 min at 100 Hz by means of a sieve shaker

144 (Retsch AS200). The dust suspension in the flask was injected into the chamber by flushing with N_2 at

145 10 L min^{-1} for about 10–15 min. After injection in the chamber, the largest fraction of the dust aerosol

146 (>1.5 μm diameter) remained in suspension for approximately 60 to 120 min thanks to a four–blade

147 stainless steel fan located at the bottom of the chamber, which also ensured homogeneous conditions

148 within the chamber volume. The submicron dust fraction, instead, remained constant with time during

149 experiments, as shown in Fig. 3 reporting the timeline of the measured effective dust fine diameter. The

150 evolution of the physico–chemical and optical properties of the suspended dust was measured by dif-

151 ferent instruments connected to the chamber. The spectral particle volume dry scattering (β_{sca}) and

152 absorption (β_{abs}) coefficients were measured, respectively, by a 3–wavelength nephelometer (TSI Inc.

153 model 3563, operating at 450, 550, and 700 nm; 2 L min^{-1} flow rate, 2–s time resolution) and a 7–

154 wavelength aethalometer (Magee Sci. model AE31, operating at 370, 470, 520, 590, 660, 880 and 950

155 nm; 2 L min^{-1} flow rate, 2–min time resolution). The size distribution of aerosols was measured by

156 means of a scanning mobility particle sizer (SMPS, TSI, DMA Model 3080, CPC Model 3772; mobility

157 diameter range 0.019–0.882 μm; 2.0/0.2 L min^{-1} sheath–aerosol flow rates, 135–s time resolution), a

158 WELAS optical particle counter (OPC) (PALAS, model 2000, white light source between 0.35 and 0.70

159 μm; optical-equivalent diameter range 0.58–40.7 μm; 2 L min^{-1} flow rate, 1–min time resolution) and a

160 SkyGrimm OPC (Grimm Inc., model 1.129, 0.655 μm operating wavelength; optical-equivalent diameter

161 range 0.25–32 μm; 1.2 L min^{-1} flow rate, 6–s time resolution). Aerosol elemental and mineralogical

162 composition, including iron oxides, was derived by analysis of dust samples collected on polycarbonate

163 filters (47-mm diameter Nuclepore, Whatman, nominal pore size 0.4 μm) mounted on a custom–made

164 stainless–steel sample holder (operated at 6 L min^{-1}) for most of the duration of each experiment.

165 All instruments (size, SW optics, filters) sampled air from the chamber. To equalize the airflow extracted

166 by the different instruments, a particle–free N_2/O_2 mixture airflow was continuously injected into the

167 chamber. Inlets for all extractive measurements consisted of a stainless steel tube located inside

168 CESAM, and an external connection of silicone tubing (TSI Inc.) from the chamber to the instruments,

169 for a total length varying between 0.4 and 1.2 m. As detailed in DB17 and shown in Fig. S1 in the

170 supplement, the transmission efficiency due to aspiration and transmission in the sampling lines as a

171 function of particle diameter was estimated to calculate the effective dust fraction sensed by each in-

172 strument, taking into account the sampling flow rate, tubing diameter, tubing geometry, and particle

173 shape and density. For the nephelometer and the aethalometer, the length of the sampling line from

174 the intake point in the chamber to the instrument entrance was about 1.2 m, which resulted in a 50%

175 cutoff of the transmission efficiency at 3.9 μm particle geometric diameter and 100% cutoff at 10 μm.

176 For the filter sampling system, the length of the sampling line of about 0.5 m resulted in a 50% (100%)

177 cutoff at 6.5 μm (15 μm) particle diameter. For the WELAS, the only OPC considered for size distribution

178 in the coarse fraction (see Sect. 2.2), the 50% (100%) cutoff was reached for particles of 5 μm (8 μm)

179 diameter.

180 All experiments were conducted at ambient temperature and relative humidity <2%. In addition to over-

181 night evacuation, the chamber was manually cleaned between experiments to avoid contaminations

182 from remaining dust. Background concentrations of aerosols in the chamber were less than 2.0 μg m^{-3}

183 (that is 10^2 to 10^5 times less than the concentration of dust aerosols in suspension in the chamber

184 during experiments)

185 A flowchart of the procedure used to treat and combine optical, size, and compositional data, and the

186 algorithm for SSA and complex refractive index retrieval is shown in Fig. 1. Full details of data treatment

187 for size distribution measurements and filter compositional data are provided in DB17 and C17, and in

188 the following we only mention the main points of interest for the present paper. Full details on the data

189 treatment of the SW optical data are provided in Sect. 2.1 and 3.

190 The optical and size datasets were acquired at different temporal resolutions and then averaged over

191 compatible 10–min intervals, whereas the compositional data represent the experiment integral. The

192 SSA and complex refractive index data were retrieved both at 10–min resolution and as experiment

193 averages to relate them to both size and compositional data. Table 1 summarizes the uncertainties on

194 the measured and derived parameters described in the following.

195 **2.1 SW optical measurements**

196 **2.1.1 Aerosol scattering coefficient**

197 The aerosol scattering coefficients (β_{sca}) at 450, 550, and 700 nm are measured by the nephelometer

198 at angles between 7° and 170° and need to be corrected for the restricted field–of–view of the instru-

199 ment (truncation correction) to retrieve β_{sca} at 0°–180°. The truncation correction factor (C_{trunc}), i.e., the

200   ratio of the β_{sca} at 0°–180° and 7°–170°, was estimated by Mie calculations for homogeneous spherical

201   particles using the size distribution measured simultaneously behind SW inlets (see Sect. 2.2). In the

202   calculations, the real part of the complex refractive index of dust was assumed to be wavelength–inde-

203   pendent and fixed at a value of 1.53, while the imaginary part was set to 0.003 at 450 and 550 nm and

204   to 0.001 at 700 nm, according to pre–existing information (Sinyuk et al., 2003; Schladitz et al., 2009;

205   Formenti et al., 2011; Rocha–Lima et al., 2018). For the different dust samples, C_{trunc} ranged between

206   1.2 and 1.7 and decreased with wavelength and the dust residence time in the chamber, following the

207   relative importance of the coarse component in the dust population (Anderson and Ogreen, 1998). The

208   uncertainty on C_{trunc}, calculated by repeating the optical calculations by using the size distribution of

209   dust within its error bars as input to the optical code, is less than ±5% at all wavelengths (in the approx-

210   imation of Mie spherical and homogeneous particles). In order to assess the consistency of the derived

211   truncation correction, we made a sensitivity study in which we recalculated C_{trunc} by varying the refrac-

212   tive index at input to Mie calculations in the range of n and k values obtained in this study (i.e., values

213   at the 10% and 90% percentile as reported in Table 5 for the whole dataset, that is n between 1.49 and

214   1.54 and k between 0.001 and 0.006 at 450, 550, and 700 nm). The results of this sensitivity study

215   indicate that, for fixed dust size distribution, the truncation correction C_{trunc} varies less than 1% for n

216   between 1.49 and 1.54, and <5% for k between 0.001 and 0.006, and so that it is quite insensitive to

217   the exact assumed n and k values.

218   Once corrected for truncation, the spectral β_{sca} was extrapolated at the aethalometer wavelengths. With

219   this aim, the Scattering Ångström Exponents, $SAE_{450-550}$ and $SAE_{550-700}$, were calculated as the linear

220   fit of β_{sca} vs λ at 450–550 nm and 550–700 nm, respectively. The $SAE_{450-550}$ and $SAE_{550-700}$ coefficients

221   were used to extrapolate β_{sca} at wavelengths respectively lower and higher than 550 nm. Extrapolated

222   β_{sca} values were used to derive an average SAE of dust for the entire investigated spectral range.

223   **2.1.2 Aerosol absorption coefficient**

224   The aerosol absorption coefficient (β_{abs}) at 370, 470, 520, 590, 660, 880, and 950 nm was retrieved

225   from aethalometer measurements. The aethalometer measures the attenuation (ATT) through an aer-

226   osol–laden quartz filter, related to the spectral attenuation coefficient (β_{ATT}) as:

227
$$\beta_{ATT}(\lambda) = \frac{\Delta ATT(\lambda)}{\Delta t} \frac{A}{V} \quad (1)$$

228   where A is the area of the aerosol collection spot (0.5 ± 0.1) cm^2 and V the air sample flow rate (0.002

229   m^3 min^{-1}). The slope $\dfrac{\Delta ATT(\lambda)}{\Delta t}$ is the linear fit of the measured attenuation as a function of time calcu-

230   lated over 10–min intervals. The spectral attenuation coefficient was converted into an absorption co-

231   efficient β_{abs} following the formula by Collaud Coen et al. (2010):

232
$$\beta_{abs}(\lambda) = \frac{\beta_{ATT}(\lambda) - \alpha(\lambda)\beta_{sca}(\lambda)}{C_{ref}R(\lambda)} \quad (2)$$

233 The $\alpha(\lambda)\beta_{sca}(\lambda)$ term accounts for the fraction of the measured attenuation due to side and backward

234 scattering and not to light absorption. The Collaud–Coen correction scheme has been recently shown

235 to yield quite accurate values of the absorption coefficients and absorption Ångström exponents from

236 aethalometer data (Saturno et al., 2017). The value of $\alpha(\lambda)$ was calculated with the formula by Arnott et

237 al. (2005) and varied between 0.002 and 0.02 (<±1% from formal error propagation on the Arnott for-

238 mula), while $\beta_{sca}(\lambda)$ is the scattering coefficient from the nephelometer extrapolated to the aethalometer

239 wavelengths. C_{ref} accounts for multiple scattering by the filter fibers, aerosol laden or not. Its spectral

240 value, obtained by the linear extrapolation of C_{ref} at 450 and 660 nm estimated for mineral dust by Di

241 Biagio et al. (2017b), varied between 4.30 at 370 nm to 3.32 at 950 nm. We assume for the extrapolated

242 C_{ref} an uncertainty of ±10% as estimated in Di Biagio et al. (2017b). The correction factor, R, accounts

243 for the decrease in the aethalometer sensitivity with the increase of the aerosol filter loading. The value

244 of R depends on the absorptivity properties of the sampled aerosol and can be calculated as a function

245 of the particle SSA. In this study, we calculated R by estimating a first–guess SSA^* as the ratio of the

246 nephelometer-corrected β_{sca} and β_{ext} obtained as the sum of β_{sca} and the β_{abs} non–corrected for filter

247 loading effect. The R was estimated by using the Collaud–Coen et al. (2010) formulation. For the range

248 of estimated SSA^* (about 0.60 to 0.99), R varied between 0.5 and 1.0 (±1–10%).

249 The Absorption Ångstrom Exponent (AAE) was calculated as the power–law fit of β_{abs} versus λ.

250 Due to an instrumental problem, aethalometer data were not always available, with a typical 30–min

251 interruption usually 10 to 30 minutes after the beginning of experiments.

252 **2.2 Size distribution**

253 The aerosol number size distribution was obtained from SMPS, WELAS and SkyGrimm measurements

254 over different diameter ranges. The measured electrical mobility and optical equivalent diameters from

255 the SMPS and the OPCs were first converted into geometrical diameters (D_g) as described in DB17

256 and summarized in Table 1. The OPCs conversion assumes for dust a complex refractive index that in

257 our study was set in the range 1.47–1.53 for n and 0.001–0.005 for k for both the SkyGrimm and the

258 WELAS (following DB17). After conversion, the estimated D_g range was 0.01–0.50 µm for the SMPS,

259 0.65–73.0 µm for the WELAS, and 0.29–68.2 µm for the SkyGrimm. Due to a calibration issue, data for

260 the SkyGrimm in the range $D_g > 1$µm were discarded, so that the WELAS is the only instrument consid-

261 ered in the super–micron range. A very low counting efficiency was observed for the WELAS below 1

262 µm and data in this size range were also discarded.

263 The SMPS, WELAS, and SkyGrimm data were combined, as detailed in DB17, to obtain the full size

264 distribution of the dust aerosols suspended in the CESAM chamber, $(dN/dlogD_g)_{CESAM}$, and the size

265 distribution behind SW optical instruments inlets, $(dN/dlogD_g)_{SWoptics}$, after taking into account particle

266 losses along sampling lines (see Supplementary material and Fig. S1). As previously discussed, due

267 to the particle losses in the sampling line from the chamber to the nephelometer/aethalometer, the

268 $(dN/dlogD_g)_{SWoptics}$ size distribution is cut at 10 µm, so no particles above this diameter reach the SW

269 instruments.

270 The measured size distributions, $(dN/dlogD_g)_{CESAM}$ and $dN/dlogD_g)_{SWoptics}$, were used to estimate the

271 mass concentration of aerosols and their effective diameter (D_{eff}) in the CESAM chamber and behind

272 the SW instrument inlets as:

273
$$\text{Mass concentration} = \int \frac{\pi}{6} D_g^3 \frac{dN}{dlogD_g} \rho \cdot dlogD_g \qquad (3)$$

274
$$D_{eff} = \frac{\int D_g^3 \frac{dN}{dlogD_g} dlogD_g}{\int D_g^2 \frac{dN}{dlogD_g} dlogD_g} \qquad (4)$$

275 The effective dust density ρ in Eq. (3) was set at 2.5 g cm^{-3}, a value that is approximately in the middle

276 of the range of desert dust densities reported in the literature, i.e., 2.1–2.75 g cm^{-3} (Maring et al., 2000;

277 Iwasaka et al., 2003; Reid et al., 2003). The effective diameter was evaluated separately for the fine

278 and coarse fractions of dust by integrating Eq. (4) for diameters ≤1 μm ($D_{eff,fine}$) and >1 μm ($D_{eff,coarse}$),

279 respectively.

280 The dust size distribution, $(dN/dlogD)_{SWoptics}$, measured at each 10–min time step for each sample was

281 fitted with a sum of five lognormal functions. For each mode, the parameters of the lognormal functions,

282 i.e., the total number concentration (N_i), the geometric median diameter ($D_{g,i}$), and the geometric stand-

283 ard deviation of the distribution (σ_i), were retrieved. The uncertainties in the retrieved parameters were

284 estimated by repeating the fit using size data within their uncertainties. The resulting parameters of the

285 fits at the peak of the injection in the chamber are reported in Table S1, and an example of size fitting

286 is shown in Fig. S2.

287 The procedure described here to estimate $(dN/dlogD_g)_{CESAM}$ and $(dN/dlogD_g)_{SWoptics}$ implies that as-

288 sumptions are made on the values of n and k to correct OPCs data, and this may introduce a circularity

289 in the estimates of the refractive index of dust that use $(dN/dlogD_g)_{SWoptics}$ as input in optical calculations

290 (see Sect. 3.2). In order to analyze the dependence of the results on this assumption, we made a

291 sensitivity calculation by varying the values of n and k used for OPCs corrections within the range of

292 values retrieved in this study (10% and 90% percentiles in Table 5, i.e., 1.49–1.54 for n and 0.001–

293 0.006 for k). We concluded that changing n and k in this range has a very low impact on the retrieved

294 number size distribution behind the SW inlets $(dN/dlogD_g)_{SWoptics}$ compared to the original assumptions

295 made in our calculations (<5% changes in the retrieved size number distribution at the different diame-

296 ters between the original correction and the correction by varying n and k). This is due to the fact that

297 when changing D_g due to changes in the n and k in the OPCs correction, the loss function also modifies

298 to values corresponding to the new D_g. Given that the loss function increases/decreases for increas-

299 ing/decreasing D_g, the combined changes in D_g and the loss function compensate so that the net num-

300 ber concentration behind the SW inlets varies less than a few percent. These results therefore suggest

301 that the procedure to estimate the complex refractive index of dust is nearly independent of the assumed

302 OPC correction.

303 **2.3 Dust elemental and mineralogical composition and iron content**

304   The elemental and mineralogical composition of the dust aerosols was estimated by combining different

305   techniques: X–ray diffraction (XRD, Panalytical model Empyrean diffractometer) to estimate the parti-

306   cles' mineralogical composition in terms of clays, quartz, calcite, dolomite, gypsum, and feldspars;

307   wavelength dispersive X–ray fluorescence (WD–XRF, Panalytical PW–2404 spectrometer) to deter-

308   mine the dust elemental composition (Na, Mg, Al, Si, P, K, Ca, Ti, Fe); and X–ray absorption near–edge

309   structure (XANES) to retrieve the content of iron oxides and their speciation between hematite and

310   goethite. The dust mass collected on Nuclepore filters during the experiments varied between 0.3 and

311   6 mg m^{-3} as calculated from elemental concentrations according to Lide (1992).

312   Full details on the XRD, WD–XRF, and XANES measurements and data analysis are provided in DB17

313   and C17. In this study, we discuss the dust elemental iron mass concentration, $MC_{Fe\%}$, i.e., the percent

314   mass of elemental iron with respect to the total dust mass concentration, and the iron oxides mass

315   concentration, $MC_{Fe-ox\%}$, i.e., the percent mass fraction of iron oxides with respect to the total dust mass

316   concentration, estimated as the sum of goethite ($MC_{Goet\%}$) and hematite ($MC_{Hem\%}$) species.

317   **3. Strategy for data analysis**

318   **3.1 Calculation of the spectral extinction coefficient and SSA from scattering and absorption**

319   **coefficients**

320   The spectral scattering and absorption coefficients, $\beta_{sca}(\lambda)$ and $\beta_{abs}(\lambda)$, measured by the nephelometer

321   and the aethalometer were used to estimate 10–min averages of the spectral extinction coefficient, β_{ext}

322   (λ), at the 7–λ of the aethalometer between 370 and 950 nm as:

323    $$\beta_{ext}(\lambda) = \beta_{abs}(\lambda) + \beta_{sca}(\lambda) \qquad (5).$$

324   The Extinction Ångström Exponent (EAE) was calculated as the power–law fit of β_{ext} versus λ.

325   The spectral single scattering albedo of dust at 10–min resolution (SSA_{10-min}) was retrieved as:

326    $$SSA_{10\text{-}min}(\lambda) = \frac{\beta_{sca}(\lambda)}{\beta_{ext}(\lambda)} \qquad (6).$$

327   The experiment–averaged SSA (λ) was calculated for each soil type based on the following formula

328   (Moosmüller et al., 2012):

329    $$SSA(\lambda) = \left(1 + \frac{1}{m(\lambda)}\right)^{-1} \qquad (7)$$

330   where m (λ) represents the slope of the linear fit between the 10–min averages of $\beta_{sca}(\lambda)$ and $\beta_{abs}(\lambda)$

331   measured along the whole duration of each experiment. An example of $\beta_{sca}(\lambda)$ versus $\beta_{abs}(\lambda)$ fitting to

332   retrieve the spectral SSA is shown in Fig. S3 in the Supplement. The correlation coefficient R^2 of the

333   β_{sca} versus β_{abs} fit usually ranges between 0.97 and 1 at all wavelengths. As will be discussed later in

334   the paper, the single scattering albedo of dust depends on the particle coarse size fraction, and during

335   our experiments SSA_{10-min} was not derived continuously for the different samples due to the aethalom-

336   eter measurement interruptions. The application of Eq. (7) avoids any bias in the calculated averaged

337   SSA for different soils due to size effects. For two of the analyzed samples (Tunisia and Namib–2),

338 however, the linear fitting procedure was not applicable due to the fact that, respectively, only two and

339 one absorption measurements from the aethalometer were available just after the peak of the injection,

340 with no data afterwards. Average SSA data for Tunisia were thus estimated as the mean of the two

341 available SSA_{10-min} data points, while the single SSA_{10-min} measurement at the peak of the injection was

342 reported for Namib–2. This difference in time sampling should be kept in mind when comparing SSA

343 data for these two samples to the rest of the dataset.

3.2 Retrieval of the spectral complex refractive index

345 An optical calculation was performed to estimate the complex refractive index (m=n–ik) of dust aerosols

346 based on optical and size data. The retrieval algorithm consisted in recalculating the spectral scattering

347 β_{sca} (λ) and absorption β_{abs} (λ) coefficients measured at each 10–min interval by using the fitted

348 $(dN/dlogD)_{SWoptics}$ size distribution as input and by varying the real and imaginary parts of the complex

349 refractive index in the calculations until the best agreement between measurements and calculations

350 was found. At each wavelength the root mean square deviation (RMSD) was calculated as:

$$RMSD(\lambda) = \sqrt{\left[\frac{\beta_{sca,measured}(\lambda) - \beta_{sca,calculated}(\lambda)(n,k)}{\beta_{sca,calculated}(\lambda)(n,k)}\right]^2 + \left[\frac{\beta_{abs,measured}(\lambda) - \beta_{abs,calculated}(\lambda)(n,k)}{\beta_{abs,calculated}(\lambda)(n,k)}\right]^2}$$

(8)

353 The RMSD was minimized at each wavelength to obtain n–k pairs that most closely reproduce the

354 measured scattering and absorption coefficients. Optical calculations were performed at the 7 wave-

355 lengths of the aethalometer between 370 and 950 nm using Mie theory for homogeneous spherical

356 particles. In the calculations, the real part of the refractive index was varied in the range 1.40–1.60 at

357 steps of 0.01, while the imaginary part was varied in the range 0.0001–0.050 at steps of 0.0001. For

358 each sample, this resulted in 10500 computations per wavelength and per 10–min time step. The un-

359 certainty on the real and imaginary parts of the refractive index was estimated with a sensitivity study.

360 For this purpose, the values of n and k were also obtained by using as input the observed β_{sca} (λ), β_{abs}

361 (λ), and $(dN/dlogD)_{SWoptics}$, plus or minus one standard deviation on their measurement. The deviations

362 of the values of n and k retrieved in the sensitivity study with respect to those obtained in the first

363 inversions were assumed to correspond to the one standard deviation uncertainty of 10–min retrieved

364 values.

365 Experiment–averaged values of the spectral n and k were estimated as the average of single n and k

366 values retrieved at 10–min steps (indicated as n_{10-min} and k_{10-min}). In fact, differently from the SSA, the

367 refractive index did not seem to depend on the particle coarse size fraction (Sect. 4.5).

368 A control experiment was performed with submicron ammonium sulphate aerosols (see DB17 and sup-

369 plementary Fig. S4) with the aim of validating the proposed methodology to estimate the aerosol com-

370 plex refractive index for a non–absorbing aerosol type. For ammonium sulphate particles with a mono–

371 modal size distribution centered at 0.06 μm, as measured with the SMPS, the retrieved real part of the

372 refractive index was 1.56 (±0.01) in the 450–700 nm wavelength range, as expected from literature

373 (Toon et al., 1976; Flores et al., 2009; Denjean et al., 2014).

3.3 Assumptions on the retrieval of SSA and complex refractive index

The approach used to retrieve the SSA and the complex refractive index of dust and the accuracy of the results depend on the accuracy of the input data and the assumptions in the optical calculations. We discuss here two points of the applied procedure, in part already mentioned in the previous paragraphs.

1/ The size distribution from OPCs and also the scattering coefficient from the nephelometer used as input to the n and k retrieval procedure and SSA calculation depend more or less directly on the dust refractive index. These instruments need in fact to be corrected for instrumental artefacts and these corrections require an a priori knowledge of the n and k, which in our approach were set to fixed values (1.47–1.53 for n and 0.001–0.005 for k for OPCs optical to geometrical diameter conversion, and 1.53 for n and 0.001–0.003 for k for nephelometer truncation correction). This choice may in principle introduce a certain degree of uncertainty and circularity into the derived n, k, and SSA for dust. Nonetheless, we note that the range of refractive index values used to correct OPCs and nephelometer data falls in the range of variability of the refractive index values obtained in this study (see Sect. 4.3), which suggests that the values used for the corrections are appropriate. Additionally, as previously discussed, both the size distribution $(dN/dlogD_g)_{SWoptics}$ and the scattering coefficient are not very sensitive to the assumptions about n and k used for the calculations (less than 5% changes in both the number size distribution behind SW inlets and the scattering coefficient from changing n and k within the range of estimated values in this study) which further demonstrates the robustness of the proposed approach.

2/ The retrieval procedure for n and k, as well as the calculations for OPCs optical–to–geometrical diameter and the nephelometer truncation correction, simplifies the non–spherical heterogeneous dust aerosols (e.g., Chou et al. 2008; Okada et al., 2011; Nousiainen and Kandler, 2015) into homogeneous spherical particles that can be represented by Mie theory. In the present study, we decided not to use a more advanced shape–representing theory, given that the shape distribution and morphology of the dust samples was not measured during experiments. Improper assumptions on the particle shape and morphology may in fact induce even larger errors than using Mie theory, in particular for super–micron aerosols (Kalashnikova and Sokolik, 2004; Nousiainen and Kandler, 2015). It should be pointed out, however, that dust is usually assumed to be spherical in global climate models (e.g., Myhre and Stordal, 2001; Balkanski et al., 2007; Jin et al., 2016), and different studies still show contrasting results on the true impact of dust non–sphericity on radiative fluxes and heating rates from global model simulations (Mishchenko et al., 1995; Yi et al., 2011; Räisänen et al., 2012; Colarco et al., 2014). On the other hand, shape effects can be important for the retrieval of aerosol properties from remote sensing techniques using spectral, angular, and polarized reflectance measurements (e.g., Feng et al., 2009).

4. Results

Nineteen soil samples from different desert areas in Northern Africa, Sahel, Eastern Africa and the Middle East, Central Asia, Eastern Asia, North America, South America, Southern Africa, and Australia were selected for experiments from a collection of 137 soil samples from source areas worldwide. The main information on the provenance of these soils is provided in Table 2. The nineteen selected soils, the same as analyzed in DB17, represent the major dust source regions depicted in Ginoux et al. (2012).

413   Amongst the database of 137 samples from all the world regions that constitute significant dust emitters,

414   this range in mineralogical composition represents the largest variability in iron oxides contents that can

415   be found worldwide. This is illustrated in Fig. 2 where we represent the variability of hematite and goe-

416   thite content in the nineteen selected soils and compare it with the range of variability of the global

417   desert soils from the database of Journet et al. (2014).

418   **4.1 Physical and chemical properties of analysed dust samples**

419   **4.1.1 Dust mass concentration and size distribution**

420   Figure 3 shows a typical example of a time series of aerosol mass concentration and effective fine and

421   coarse diameters measured inside the CESAM chamber and behind the SW instruments inlets during

422   the experiments, as well as the corresponding β_{sca} and β_{abs} at 370 nm. The Figure shows the rapid

423   increase of the mass concentration within CESAM during dust injection in the chamber, and its subse-

424   quent decrease during experiments due to both size–selective gravitational settling, occurring mostly

425   within the first 30 min of experiments, and dilution by sampling. The scattering and absorption coeffi-

426   cients of dust decrease with time after injection in tandem with the decrease of the mass concentration

427   and the size–dependent depletion in the chamber. The dust mass concentration inside CESAM at the

428   peak of the injection is between 2 mg m^{-3} (Mali) and 310 mg m^{-3} (Bodélé) and falls to values between

429   0.9 mg m^{-3} (Mali) and 20 mg m^{-3} (Bodélé) behind SW instruments inlets. These values are comparable

430   to those measured close to sources during dust storms (Rajot et al., 2008; Kander et al., 2009). After a

431   2–hour experiment, the dust mass concentration has decreased to values of 0.2 to 2.5 mg m^{-3} (inside

432   CESAM) and of 0.1 to 1.9 mg m^{-3} (behind the SW inlets), within a range of values comparable to what

433   has been measured after medium– to long–range dust transport in the real atmosphere (Weinzerl et

434   al., 2011; Denjean et al., 2016b). These data therefore indicate that in a 2–hour experiment in CESAM

435   it is possible to reproduce the temporal changes of the mass load observed in the real atmosphere for

436   dust from its emission to a receptor site.

437   Concurrently with the mass concentration, the effective diameter, $D_{eff,coarse}$, of the coarse fraction of the

438   dust aerosol also rapidly decreases with time due the progressive deposition of the coarsest particles

439   in the chamber. For the different analyzed soils, $D_{eff,coarse}$ varies in the range of 4–8 µm (peak of injection)

440   to 3–4 µm (after 2 hours) inside the CESAM chamber, and in the range of 3–4 µm (peak of injection) to

441   2–3 µm (after 2 hours) behind the SW inlets. In contrast, $D_{eff,fine}$ remains quite constant during the ex-

442   periments, with a value between 0.6 and 0.7 µm for all soils. The values of $D_{eff,coarse}$ obtained in this

443   study inside the CESAM chamber are in line with those measured close to African sources (4–12 µm,

444   Rajot et al., 2008; Weinzerl et al., 2009; Ryder et al., 2013a) and for dust transported across the Medi-

445   terranean (5–8 µm, Denjean et al., 2016a). Conversely, the values of $D_{eff,coarse}$ behind the SW instru-

446   ments inlets are mostly in agreement with those reported for dust transported across the Atlantic ocean

447   (~3 µm, Maring et al., 2003; Müller et al., 2011; Denjean et al., 2016b). Our values of $D_{eff,fine}$ are higher

448   compared to values reported by Denjean et al. (2016a) for dust aerosols transported over the Mediter-

449   ranean (0.2 to 0.5 nm), reflecting the fact that we analyse pure dust whereas these authors often en-

450   countered dust externally mixed with pollution particles.

451 The comparison of $D_{eff,coarse}$ values suggests that while the size of dust in CESAM is mostly representa-
452 tive of dust close to sources, as already pointed out in DB17, the size measured behind the SW instru-
453 ments inlets is mostly representative of transport conditions. Figure 4 illustrates this point by showing
454 the volume size distributions of the generated dust aerosols at the peak of injection seen by the SW
455 optical instruments, compared to the average size of dust measured in CESAM (DB17) and field obser-
456 vations close to sources (e.g., Niger) and after long–range transport (Cape Verde, Suriname, and
457 Puerto Rico). The size distribution of dust inside CESAM includes a coarse mode up to tenths of micro-
458 metres and well reproduces field observations close to sources, as shown in comparison to the Niger
459 case. Due to particle losses along tubes, the coarsest particles above 10 µm diameter are not seen by
460 the SW instruments. The overall shape of the dust size distribution sensed by the SW instruments is
461 comparable to that measured during atmospheric long–range transport, even if the fraction of particles
462 above 10 µm diameter is significantly under–represented compared to observations. (i.e., Betzer et al.,
463 1988; Formenti et al., 2001; Maring et al., 2003; Ryder et al., 2013b; Jeong et al., 2014; Denjean et al.,
464 2016b).

4.1.2 Iron and iron oxide dust content

466 The mass concentrations of iron oxides, hematite, goethite, and total elemental iron for the different
467 analysed samples are reported in Table 3. There is a considerable variability in the iron and iron oxide
468 content for our samples. Total iron in the dust samples is in the range from 2.4% (Namib–1) to 10.6%
469 (Australia). Iron oxides account for 11% and 62% of the iron mass, whereas the percent of iron oxides
470 to the total dust mass varies between 0.7% (Bodélé Depression) and 5.8% (Niger). These data are in
471 the range of values reported in the literature (Reid et al., 2003; Scheuvens et al., 2013; Formenti et al.,
472 2011, 2014a). For the samples from the Sahara and the Sahel, goethite is the dominant iron oxide
473 species, in agreement with Lafon et al. (2006) and Formenti et al. (2014a; 2014b). In contrast, over
474 other regions, hematite dominates over goethite, as already reported by some studies (Arimoto et al.,
475 2002; Shen et al., 2006; Lu et al., 2011).

4.2 Spectral– and time–dependent dust extinction and absorption coefficients, complex refrac-
tive index, and SSA

478 Figure 5 illustrates a typical spectral– and time–dependent set of measured optical properties. The
479 spectral extinction coefficient, absorption coefficient, SSA, and real and imaginary parts of the complex
480 refractive index obtained at 10–min resolution for the Morocco and Algeria samples are shown at the
481 peak of the dust injection in CESAM and 30 and 90 min after the peak. Figure 5 shows that absorption
482 decreases with wavelength, but not extinction. The SSA increases from 370 to 590 nm while it shows
483 almost constant values between 590 and 950 nm. The imaginary refractive index decreases with λ
484 following the decrease of β_{abs}. The real part of the refractive index is almost constant with wavelength.

485 The extinction and absorption coefficients decrease in absolute value with time, as already shown in
486 Fig. 3, but their spectral dependence remains quite constant with time, even if it varies from soil to soil.
487 The experiment–averaged Absorption, Scattering, and Extinction Ångström Exponents, representing
488 the spectral variation of the absorption, scattering and extinction coefficients, vary between the values
489 of 1.5 and 2.4 (AAE), −0.4 and 0.4 (SAE), and −0.2 and +0.5 (EAE) for the different samples. These

490 values are in line with those previously reported by Moosmüller et al. (2012) and C17 for dust from
491 various locations. The retrieved n and k also show negligible changes of their spectral shape with time
492 and their magnitude remains approximately constant. In contrast, the SSA increases with time, in par-
493 ticular below 600 nm wavelength, and so its spectral shape changes. This is mostly due to the decrease
494 of the coarse size fraction with residence time in the chamber, as will be analysed in Sect. 4.5. Similarly
495 to the absorption, scattering, and extinction coefficients, the spectral shape of k and SSA is somewhat
496 different between the various samples, with the sharpest spectral variations observed for the most ab-
497 sorbing samples and a less pronounced spectral variation for the less absorbing ones, as evident, for
498 example, by comparing the SSA data for Morocco and Algeria in Fig. 5.

499 4.3 Spectral complex refractive index and SSA for the different source regions and comparison
500 to literature data

501 Figure 6 shows the experiment–averaged n, k, and SSA between 370 and 950 nm for the nineteen
502 aerosol samples analyzed in this study. Data of n, k, and SSA and their uncertainties for each sample
503 are reported in Tables 4 and 5 together with the average values for each of the eight different source
504 regions and for the full dataset. Figure 6 shows that there are significant differences, both in magnitude
505 and spectral shape, between the imaginary refractive index and SSA for the different samples. The
506 highest values of k (and lowest values of SSA) are obtained for the Niger, Mali, Namib–2 and Australia
507 samples, which also show the highest values of both the iron oxide content between 3.6% and 5.8%
508 and hematite content between 2.0% and 4.8% (k is in the range 0.0048–0.0088 at 370 nm and 0.0012–
509 0.0021 at 950 nm, and SSA is in the range 0.70–0.75 at 370 nm and 0.95–0.97 at 950 nm). The lowest
510 values are obtained for the Bodélé, Namib–1, and Arizona samples, which have iron oxide contents
511 between 0.7% and 1.5% (k is 0.001 at 370 and 0.0003 at 950 nm, and SSA is in the range 0.91–0.96
512 at 370 nm and 0.97–0.99 at 950 nm). Both k and SSA vary from region to region, with the largest
513 absorptions (highest k, lowest SSA) for the Sahel and Australia and the lowest absorption (lowest k,
514 highest SSA) in North and South America and the Middle East; k and SSA values also vary within the
515 same region, as illustrated in Fig. 6 for the Sahelian and Southern African samples. The real part of the
516 refractive index, on the other hand, is not only almost wavelength–independent, as anticipated, but also
517 relatively invariant from sample to sample. Its average over the 370–950 nm spectral range is between
518 1.48 (Gobi) and 1.55 (Ethiopia and Namib–2).

519 The full envelope of n, k, and SSA obtained for the entire set of analysed samples is shown in Fig. 7a
520 and 7b (left panels). The real refractive index is relatively invariant, the spectral k varies by up to an
521 order of magnitude (0.001–0.009 at 370 nm and 0.0003–0.002 at 950 nm). The SSA changes accord-
522 ingly for the different dust samples at the different wavelengths (30% change at 370 nm corresponding
523 to values between 0.70–0.96 and 4% change at 950 nm for values within 0.95–0.99). The population
524 mean is 1.52 for n (as spectral average) and varies in the range 0.0033–0.0009 for k and 0.85–0.98 for
525 the SSA between 370 and 950 nm (0.0016 and 0.94 as spectral averages for k and SSA) (Fig. 7 and
526 Tables 4 and 5).

527 The comparison between the full envelope of n, k, and SSA in this study with literature data is shown
528 in Fig. 7a and 7b (right panels). Literature values considered for comparison include estimates from

529   ground–based, aircraft, and satellite observations, laboratory studies, AERONET inversions, and esti-
530   mates from mixing rules based on the dust mineralogical composition. Given that the sample selection
531   in our experiments fully envelopes the global variability of mineralogy of natural dust, we could expect
532   that our dataset would also fully envelope the global-scale variability of the dust absorption and scat-
533   tering properties in the SW. When comparing with available literature data we found that our n and SSA
534   datasets very well envelope the range of values indicated in the literature, with only a few outlier points.
535   In contrast, for the imaginary refractive index the reported range of variability from the literature is sig-
536   nificantly larger than that found in our study, with our range of k being mostly at the lower bound of
537   previous results. Nonetheless, our range of k values fully envelopes the ensemble of remote sensing
538   and field campaign data on airborne dust from the previous literature reported in Fig. 7a. The global
539   average spectral values for k in our study (thick black line) perfectly match the Dubovik et al. (2002)
540   dataset from a synthesis of AERONET observations from various locations worldwide. Likewise, our k
541   average is also very close to the dataset by Balkanski et al. (2007), estimated from mineralogical com-
542   position assuming 1.5% in volume of hematite in dust (a value similar to our population average of 1.8%
543   (in mass) for the dust hematite content), a value shown to allow a reconciliation of climate modelling
544   and satellite observations of the dust direct SW radiative effect. Looking at Fig. 7a, the datasets which
545   show the largest deviations from our estimated range of k are the ones by: (i) Volz (1972), Patterson et
546   al. (1977) and Hess et al. (1998; i.e., the OPAC database, which is the same k dataset used in the new
547   OPAC 4.0 version, Koepke et al., 2015), which are also amongst the most commonly used references
548   for the dust imaginary refractive index in many climate models; (ii) the dataset by Wagner et al. (2012),
549   from laboratory chamber experiments; and (iii) the dataset by Steigmann and Yang (2017), estimated
550   from a machine learning technique. The reasons for these discrepancies in the k values are difficult to
551   assess, since they can be related to both instrumental and analytical aspects. In the studies by Volz
552   (1972) and Patterson et al. (1977), for instance, the complex refractive index was obtained by transmit-
553   tance and diffuse reflectance on pellet samples, a technique that requires the dust to be pressed in a
554   matrix of non–absorbing material. In this case a discrepancy arises from the different optical behaviour
555   between dust compressed in a pellet and the airborne particles. Moreover, Volz (1972) and Patterson
556   et al. (1977) analyse dust aerosols collected after mid– to long– transport, so after the dust have been
557   possibly mixed with absorbing species. For the case of Wagner et al. (2012), the choice of the optical
558   theory to retrieve k (T–matrix instead of Mie theory as used in our work, but also used in the majority of
559   past field and remote sensing literature studies considered) is expected to cause the observed differ-
560   ences with our dataset.

561   **4.4 Imaginary refractive index and SSA versus iron and iron oxide content**

562   The sample–to–sample variability of the imaginary part of the refractive index k and the SSA observed
563   in Fig. 6 and 7 is related to the dust composition by investigating the dependence on the particle iron
564   content. In Fig. 8 we show the experiment–averaged k and SSA at 370, 520, and 950 nm versus the
565   mass concentration of iron oxides (hematite+goethite, $MC_{Fe-ox\%}$), hematite ($MC_{Hem\%}$), goethite
566   ($MC_{Goeth\%}$), and total elemental iron ($MC_{Fe\%}$) measured for the different dust samples analyzed in this
567   study. The data are linearly fitted to relate k and SSA to $MC_{Fe\%}$, $MC_{Hem\%}$, $MC_{Goeth\%}$, and $MC_{Fe\%}$. The
568   results of the fits at all wavelengths between 370 and 950 nm are reported in Table 6, together with the

569 statistical indicators of the goodness of fit (correlation coefficient, R^2, and reduced chi square, χ^2_{red}, i.e.,
570 the obtained chi square divided by the number of degrees of freedom). The data in Fig. 8 and Table 6
571 indicate that there is an excellent correlation between both k and SSA and $MC_{Fe-ox\%}$ at the different
572 wavelengths ($R^2 > 0.75$). A weaker correlation is found when relating k and SSA to $MC_{Hem\%}$ and $MC_{Fe\%}$
573 (R^2 between 0.40 and 0.74 for k and between 0.49 and 0.78 for the SSA), and $MC_{Goeth\%}$ (R^2 between
574 0.17 and 0.62). The better correlation of k and SSA to $MC_{Fe-ox\%}$ compared to $MC_{Fe\%}$ is expected since
575 dust optical properties in the visible wavelengths are mostly sensitive to the fraction of iron oxides,
576 rather than to iron incorporated into the crystal structure of silicates (i.e., Karickhoff and Bailey, 1973;
577 Lafon et al., 2006; Moosmüller et al., 2012; Klaver et al., 2011; Engelbrecht et al., 2016; C17). The
578 quantities that most robustly satisfy a linear relationship are k and $MC_{Fe-ox\%}$, as indicated by the reduced
579 chi square χ^2_{red} that is around 1 at all different wavelengths. The χ^2_{red} increases to values also larger
580 than 2 in the other cases, indicating the poorer robustness of the fit in these cases.

581 We also investigated the dependence of the spectral k and SSA on the mass concentration of other
582 minerals contained in dust, such as clays, calcite, quartz, and feldspars, and also on the mass concen-
583 tration of different elements. We found that there is no statistically significant correlation between k and
584 SSA and the mass concentration of any of these compounds (not shown), with R^2 values between 0.002
585 and 0.46 at the different wavelengths for all cases.

586 These results therefore clearly show that iron, particularly in the form of iron oxides, is the main driver
587 of dust shortwave absorption.

588 **4.5 Imaginary refractive index and SSA versus dust coarse size fraction**

589 The dependence of the spectral k and SSA on the dust coarse fraction is investigated by relating it to
590 the $D_{eff,coarse}$ calculated from the size distribution data behind the SW instruments inlets. The k_{10-min} and
591 SSA_{10-min} at 370, 520, and 950 nm versus $D_{eff,coarse}$ are shown in Fig. 9 for all experimental data, which
592 we separated into three classes based on their iron oxide content ($MC_{Fe-ox\%} \leq 1.5\%$, $1.5\% < MC_{Fe-ox\%}$
593 $< 3\%$, $MC_{Fe-ox\%} \geq 3\%$). Figure 9 shows that even if the correlation is not very strong ($R^2 < 0.54$), there is
594 a clearly decreasing tendency for the SSA_{10-min} with increasing $D_{eff,coarse}$, particularly at 370 and 520 nm
595 for strongly absorbing samples with iron oxide content larger than 3%. The SSA_{10-min} is mostly inde-
596 pendent of changes of $D_{eff,coarse}$ at 950 nm. Conversely, k_{10-min} has a very poor correlation with $D_{eff,coarse}$
597 ($R^2 < 0.35$) and thus does not depend on size. Similar results were also obtained for the real part (not
598 shown).

599 These results confirm previous observations (Sokolik and Toon, 1999; McConnell et al., 2008, 2010;
600 Kandler et al., 2011; Ryder et al., 2013a; 2013b) that the refractive index, an intrinsic property of matter,
601 is independent of size, while the SSA increases as the coarse dust size fraction decreases. This is due
602 to the fact that absorption efficiency for a single particle (Q_{abs}) increases with particle diameter while the
603 scattering efficiency (Q_{sca}) decreases. Ryder et al. (2013a) also showed that the dependence of SSA
604 on size is linear, but important only when the coarse fraction is high (if particles larger than about 3 μm
605 in diameter are present), otherwise the SSA depends mainly on composition.

606 **5. Summary and concluding remarks**

607 In this paper we presented new measurements of the spectral SW complex refractive index (m=n–ik)
608 and single scattering albedo (SSA) for nineteen mineral dust aerosols generated in the laboratory from
609 natural soil samples from major desert dust source areas in northern Africa, the Sahel, Middle East,
610 eastern Asia, North and South America, southern Africa, and Australia, and selected to represent the
611 heterogeneity of the dust composition at the global scale, in particular the range of iron oxide concen-
612 trations. The envelope of refractive indices and SSA data obtained in this study can thus be taken as
613 representative of the variability of the global dust aerosol.

614 Experiments described here were conducted in the 4.2 m^3 CESAM chamber, a realistic and dynamic
615 environment where dust aerosols can be generated and maintained in suspension for few hours while
616 monitoring the evolution of their physical, chemical, and optical properties. The generated dust aerosols
617 are characterized by a realistic size distribution, including both the sub–micron and the super–micron
618 fraction, and they have an atmospherically representative mass concentration and composition, includ-
619 ing iron oxides and elemental iron content.

620 The results of the present study can be summarized as follows:

621 1. The spectral k and SSA retrieved in this study vary from sample to sample within the same region
622 but also from a region to another. For k, values vary between 0.001–0.009 at 370 nm and 0.0003–
623 0.002 at 950 nm. For SSA, values vary from 0.70 to 0.96 at 370 nm and from 0.95 at 0.99 at 950
624 nm. In contrast, n is wavelength–independent and almost uniform for the different sources, with
625 values between 1.48 and 1.55. Values for n and SSA fall within the range of published literature
626 estimates, while for k we obtain a much narrower range of variability than the ensemble of literature
627 results, as illustrated in Fig. 7. In particular, we found lower values of k compared to most of the
628 literature values currently used in climate models, such as Volz et al. (1972), Patterson et al. (1977),
629 and the OPAC database (Hess et al., 1998; Koepke et al., 2015). Miller et al. (2014) state that the
630 values of Dubovik et al. (2002) from AERONET, Patterson et al. (1977) for far–travelled dust, and
631 OPAC probably bracket the global solar absorption by dust. In contrast, our results indicate that
632 dust absorption is lower than previously thought, and its average is close to the values reported by
633 Dubovik et al. (2002) from AERONET observations and Balkanski et al. (2007) for a dust with a
634 1.5% volume fraction of hematite. Our range of variability of an order of magnitude for k and be-
635 tween 4% and 30% for the spectral SSA is actually large enough to change the sign of the global
636 dust direct effect at the TOA (Miller et al., 2004), as well as its regional implications (e.g., Solmon
637 et al., 2008; Jin et al., 2016), and has to be taken into account in climate modelling.

638 2. The documented changes in k and SSA also impact remote sensing retrievals. To give an example,
639 following Gasteiger et al. (2011), our observed variability of about 10% for the SSA at 532 nm would
640 translate to about 40% variability in the retrieved extinction profiles and optical depths from lidar
641 observations for dust from varying sources.

642 3. The sample–to–sample variability observed in this study is mostly related to the iron oxide and
643 elemental iron content in dust. At each investigated wavelength the magnitude of k and SSA is
644 linearly correlated to the mass concentration of total iron oxides, hematite, goethite, and total ele-
645 mental iron. Small variations of these compounds translate into large variations of k and SSA. This

646   suggests that it is sufficient to know the content of iron oxide or elemental iron in dust to predict its

647   spectral k and SSA, which represents a huge simplification for parameterizing their regional and

648   global variability.

649 4. We also investigated the dependence of k and SSA on the size distribution of dust. While k is

650   independent of size (suggesting that a constant value can be used along transport), below 600 nm

651   the SSA linearly decreases for increasing $D_{eff,coarse}$ for strongly absorbing samples with more than

652   3% iron oxide content. The investigated range of $D_{eff,coarse}$ is within about 2 and 4 μm, and thus

653   comparable to values obtained along a transport path over the Atlantic Ocean for dust during about

654   2 to 6 days following emission (Denjean et al., 2016a).

655 Based on our results, we recommend that dust simulations, as well as remote sensing retrievals, use

656 source–dependent values of the spectral SW refractive index and SSA instead of generic values. We

657 propose, as a first step, a set of regionally–averaged n, k, and SSA values to represent dust from each

658 of the eight regions analysed here as well as a global average value from the ensemble of our data

659 (Tables 4 and 5). Furthermore, the relationships found between k and SSA and the iron oxides or ele-

660 mental iron content in dust open the perspective to establish predictive rules to estimate the spectrally–

661 resolved SW absorption of dust based on composition. We recommend the use of iron oxide content

662 rather than iron content as it is better correlated with k and SSA. The relationship found in this study,

663 nonetheless, refer to the bulk composition of the dust aerosols and to a size range typical of 2 to 6 days

664 of transport in the atmosphere. As demonstrated in C17 with the mass extinction efficiency, the rela-

665 tionships linking the dust absorption to iron content vary as a function of the analysed size fraction due

666 to the fact that iron bearing minerals are more concentrated in the clay fraction (<2.0 μm) than in the

667 coarsest fraction of the dust (Kandler et al., 2009; C17). Further investigation should be therefore ad-

668 dressed to evaluate the dependence of the spectral k and SSA versus iron content as a function of the

669 size distribution of the particles. This will allow to determine if the k and SSA versus iron relationships

670 change or not in different phases of the aerosol lifetime, so from the source areas (when the coarsest

671 fraction is dominant), to long–range transport conditions (when most of the coarse particle fraction

672 above few μm has settled out). We point out, however, that the use of mineralogy to estimate k and

673 SSA based on linear relationships, as obtained in our study, requires nonetheless that the model–pre-

674 dicted dust composition accurately reflects that of the natural atmospheric aerosols. To this aim, realistic

675 soil mineralogy databases and accurate modelling of the soil to aerosol size fractionation need to be

676 developed in model schemes.

677 Finally, this study had the objective to investigate the variability of the dust SW optical properties at the

678 global scale in link to the global variability of the dust composition. It is noteworthy that observations

679 over Southern Africa and the Sahel from the present study indicate that the k and SSA variabilities over

680 these regions are comparable to the ones obtained for the global scale. For other regions, such as

681 North America and Australia, only one sample was analyzed, with no information on the regional-scale

682 variability of k and SSA. Additionally, for some of the analyzed areas, such as the Bodélé depression,

683 even local scale variability (on the order of few km) may be of relevance, given the documented local

684 scale changes of the particles' mineralogy and iron content (Bristow et al., 2010). More efforts should

685   be therefore devoted to better characterize the variability of dust spectral optical properties at the re-

686   gional scale with the aim of better assessing the dust impact on the climate of different areas of the

687   world.

688

689   **Data availability**

690   Complex refractive index and single scattering albedo data for the different analyzed samples are pro-

691   vided in Tables 4 and 5. Processed CESAM data are immediately available upon request to the contact

692   author. They will also soon be made available through the EUROCHAMP–2020 data center

693   (https://data.eurochamp.org/). The following IDL routines were used in the analysis: mpfitexy.pro (avail-

694   able at https://github.com/williamsmj/mpfitexy) was used to linearly fit data taking into account uncer-

695   tainties on both x and y; mie_single.pro (available at http://www.atm.ox.ac.uk/code/mie/mie_sin-

696   gle.html) was used for optical calculations using Mie theory; mpcurvefit.pro (available at http://cow.phys-

697   ics.wisc.edu/~craigm/idl/idl.html) was used for size lognormal fitting.

698

699   **Author contributions**

700   C. Di Biagio, P. Formenti, Y. Balkanski, and J. F. Doussin designed the experiments and discussed the

701   results. C. Di Biagio performed the experiments and performed the full data analysis with contributions

702   by P. Formenti, L. Caponi, M. Cazaunau, E. Pangui, and J.F. Doussin. The soil samples used for ex-

703   periments were collected by M. O. Andreae, K. Kandler, T. Saeed, S. Piketh, D. Seibert, and E. Wil-

704   liams. E. Journet participated to the selection of the soil samples for experiments. Sophie Nowak per-

705   formed the XRD measurements. C. Di Biagio and P. Formenti wrote the manuscript with comments

706   from all co–authors.

707

708   **Acknowledgements**

709   The RED–DUST project was supported by the French national programme LEFE/INSU, by the OSU–

710   EFLUVE (Observatoire des Sciences de l'Univers–Enveloppes Fluides de la Ville à l'Exobiologie)

711   through dedicated research funding and by the CNRS–INSU by supporting CESAM as national facility.

712   This work has received funding from the European Union's Horizon 2020 research and innovation pro-

713   gramme through the EUROCHAMP–2020 Infrastructure Activity under grant agreement no. 730997.

714   This work was granted access to the HPC resources of TGCC under allocation 2018-A0050102201

715   made by GENCI. C. Di Biagio was supported by the CNRS via the Labex L–IPSL, funded by the ANR

716   (grant no. ANR–10–LABX–0018). K. Kandler is funded by the Deutsche Forschungsgemeinschaft

717   (DFG, German Research Foundation) – 264907654; 416816480 (KA 2280). Field sampling in Saudi

718   Arabia was supported by a grant from King Saud University. The authors thank the LISA staff, who

719   participated in the collection of the soil samples from Tunisia, Niger, Atacama, Patagonia, and the Gobi

720   desert used in this study, and S. Caquineau (LOCEAN), S. Chevaillier (LISA) and G. Landrot (synchro-

721   tron SOLEIL), for their contribution in the XRD, WD–XRF and XANES analyses.

References

Anderson, T. L. and Ogren, J. A.: Determining aerosol radiative properties using the TSI 3563 integrating nephelometer, Aerosol Sci. Technol., 29, 57–69, 1998.

Arimoto, R., Balsam, W., and Schloesslin, C.: Visible spectroscopy of aerosol particles collected on filters: iron–oxide minerals, Atmos. Environ., 36, 89–96, 2002.

Arnott, W., Hamasha, K., Moosmüller, H., Sheridan, P. J. , and Ogren, J. A.: Towards aerosol light-absorption measurements with a 7–wavelength aethalometer: Evaluation with a photoacoustic instrument and 3–wavelength nephelometer, Aerosol Sci. Tech., 39(1), 17–29, 2005.

Balkanski, Y., Schulz, M., Claquin, T., and Guibert, S.: Reevaluation of Mineral aerosol radiative forcings suggests a better agreement with satellite and AERONET data, Atmos. Chem. Phys., 7, 81–95, doi:10.5194/acp-7-81-2007, 2007.

Bangalath, H.K. and Stenchikov, G.: Sensitivity of the Middle East–North African Tropical Rainbelt to Dust Shortwave Absorption: A High-Resolution AGCM Experiment. J. Climate, 29, 7103–7126, https://doi.org/10.1175/JCLI-D-15-0827.1, 2016.

Betzer, P., Carder, K., Duce, R., & Merrill, J.: Long range transport of giant mineral aerosol particles. Nature, 336, 568–571, 1988.

Boucher, O., et al., Clouds and Aerosols. Stocker, T., & Qin, D. (eds), Climate Change 2013: The Physical Science Basis. Contribution of Working Group I to the Fifth Assessment Report of the Intergovernmental Panel on Climate Change. Cambridge Univ. Press, Cambridge, United Kingdom and New York, NY, USA, 2013.

Bretl, S., P. Reutter, C. C. Raible, S. Ferrachat, C. Schnadt Poberaj, L. E. Revell, and U. Lohmann: The influence of absorbed solar radiation by Saharan dust on hurricane genesis, J. Geophys. Res. Atmos., 120, doi:10.1002/2014JD022441, 2015.

Bristow, C. S., Hudson-Edwards, K. A., and Chappell, A.: Fertilizing the Amazon and equatorial Atlantic with West African dust, Geophys. Res. Lett., 37, L14807, doi:10.1029/2010GL043486, 2010.

Caponi, L., Formenti, P., Massabó, D., Di Biagio, C., Cazaunau, M., Pangui, E., Chevaillier, S., Landrot, G., Andreae, M. O., Kandler, K., Piketh, S., Saeed, T., Seibert, D., Williams, E., Balkanski, Y., Prati, P., and Doussin, J.-F.: Spectral- and size-resolved mass absorption efficiency of mineral dust aerosols in the shortwave spectrum: a simulation chamber study, Atmos. Chem. Phys., 17, 7175-7191, https://doi.org/10.5194/acp-17-7175-2017, 2017.

Carrico, C. M., P. Kus, M. J. Rood, P. K. Quinn, and T. S. Bates, Mixtures of pollution, dust, sea salt, and volcanic aerosol during ACE-Asia: Radiative properties as a function of relative humidity, J. Geophys. Res., 108, 8650, doi: 10.1029/2003JD003405, D23, 2003.

Cattrall, C., Carder, K. L., and Gordon, H. R.: Columnar aerosol single-scattering albedo and phase function retrieved from sky radiance over the ocean: Measurements of Saharan dust, J. Geophys. Res.-Atmos., 108(D9), 4287, doi:10.1029/2002JD002497, 2003

Chen, G., Ziemba, L. D., Chu, D. A., Thornhill, K. L., Schuster, G. L., Winstead, E. L., Diskin, G. S., Ferrare, R. A., Burton, S. P., Ismail, S., Kooi, S. A., Omar, A. H., Slusher, D. L., Kleb, M. M., Reid, J. S., Twohy, C. H., Zhang, H., and Anderson, B. E.: Observations of Saharan dust microphysical and optical properties from the Eastern Atlantic during NAMMA airborne field campaign, Atmos. Chem. Phys., 11, 723-740, https://doi.org/10.5194/acp-11-723-2011, 2011.

Chou, C., Formenti, P., Maille, M., Ausset, P., Helas, G., Harrison, M., and Osborne, S.: Size distribution, shape, and composition of mineral dust aerosols collected during the African Monsoon Multidisciplinary Analysis Special Observation Period 0: Dust and Biomass-Burning Experiment field campaign in Niger, January 2006, J. Geophys. Res., 113, D00C10, doi:10.1029/2008jd009897, 2008.

Claquin, T., Schulz, M., and Balkanski, Y.: Modeling the mineralogy of atmospheric dust sources, J. Geophys. Res., 104, 22 243– 22 256, 1999.

Clarke, A. D., Shinozuka, Y. V., Kapustin, N., Howell, S., Huebert, B., Doherty, S.,Anderson, T., Covert, D., Anderson, J., Hua, X., Moore II, K. G., McNaughton, C., Carmichael, G., and Weber, R.: Size distributions and mixtures of dust and black carbon aerosol in Asian outflow: Physiochemistry and optical properties, J. Geophys. Res., 109, D15S09, doi:10.1029/2003JD004378, 2004.

Colarco, P. R., Nowottnick, E. P., Randles, C. A., Yi, B., Yang, P., Kim, K.-M., Smith, J. A., and Bardeen, C. G.: Impact of radiatively interactive dust aerosols in the NASA GEOS-5 climate model: Sensitivity to dust particle shape and refractive index, J. Geophys. Res. Atmos., 119, 753–786, doi: 10.1002/2013JD020046, 2014.

Collaud Coen, M., Weingartner, E., Apituley, A., Ceburnis, D., Fierz-Schmidhauser, R., Flentje, H., Henzing, J. S., Jennings, S. G., Moerman, M., Petzold, A., Schmid, O., and Baltensperger, U.: Minimizing light absorption measurement artifacts of the Aethalometer: evaluation of five correction algorithms, Atmos. Meas. Tech., 3, 457–474, doi:10.5194/amt-3-457-2010, 2010.

d'Almeida, G. A., Koepke, P., and Shettle, E.P.: Atmospheric Aerosols: Global Climatology and Radiative Characteristics, A. Deepak Publishing, 561 pp., 1991.

Das, S., S. Dey, S. K. Dash, G. Giuliani, and F. Solmon: Dust aerosol feedback on the Indian summer monsoon: Sensitivity to absorption property, J. Geophys. Res. Atmos., 120, 9642–9652, doi: 10.1002/2015JD023589, 2015.

Denjean, C., Formenti, P., Picquet-Varrault, B., Katrib, Y., Pangui, E., Zapf, P., and Doussin, J. F.: A new experimental approach to study the hygroscopic and optical properties of aerosols: application to ammonium sulphate particles, Atmos. Meas. Tech., 7, 183-197, doi:10.5194/amt-7-183-2014, 2014.

Denjean, C., Cassola, F., Mazzino, A., Triquet, S., Chevaillier, S., Grand, N., Bourrianne, T., Momboisse, G., Sellegri, K., Schwarzenbock, A., Freney, E., Mallet, M., and Formenti, P.: Size distribution and optical properties of mineral dust aerosols transported in the western Mediterranean, Atmos. Chem. Phys., 16, 1081–1104, https://doi.org/10.5194/acp-16-1081-2016, 2016a.

Denjean, C., Formenti, P., Desboeufs, K.,Chevaillier, S., Triquet, S., Maillé, M., Cazaunau, M., Laurent, B., Mayol-Bracero, O. L., Vallejo, P., Quiñones, M., Gutierrez-Molina, I. E., Cassola, F., Prati, P., Andrews, E., and Ogren, J.: Size distribution and optical properties of African mineral dust after intercontinental transport, J. Geophys. Res.-Atmos., 121, 7117–7138, https://doi.org/10.1002/2016JD024783, 2016b.

Derimian, Y., Karnieli, A., Kaufman, Y. J., Andreae, M. O., Andreae, T. W., Dubovik, O., Maenhaut, W., and Koren, I.: The role of iron and black carbon in aerosol light absorption, Atmos. Chem. Phys., 8, 3623-3637, 2008.

Di Biagio, C., Formenti P., Styler S. A., Pangui E., and Doussin J.-F.: Laboratory chamber measurements of the longwave extinction spectra and complex refractive indices of African and Asian mineral dusts, Geophys. Res. Lett., 41, 6289-6297, doi:10.1002/2014GL060213, 2014a.

Di Biagio, C., Boucher, H., Caquineau, S., Chevaillier, S., Cuesta, J., and Formenti, P.: Variability of the infrared complex refractive index of African mineral dust: experimental estimation and implications for radiative transfer and satellite remote sensing, Atmos. Chem. Phys., 14, 11093-11116, https://doi.org/10.5194/acp-14-11093-2014, 2014b.

Di Biagio, C., Formenti, P., Balkanski, Y., Caponi, L., Cazaunau, M., Pangui, E., Journet, E., Nowak, S., Caquineau, S., Andreae, M. O., Kandler, K., Saeed, T., Piketh, S., Seibert, D., Williams, E., and Doussin, J.-F.: Global scale variability of the mineral dust long-wave refractive index: a new dataset of in situ measurements for climate modeling and remote sensing, Atmos. Chem. Phys., 17, 1901-1929, https://doi.org/10.5194/acp-17-1901-2017, 2017a.

Di Biagio, C., Formenti, P., Cazaunau, M., Pangui, E., Marchand, N., and Doussin, J.-F.: Aethalometer multiple scattering correction C_{ref} for mineral dust aerosols, Atmos. Meas. Tech., 10, 2923-2939, https://doi.org/10.5194/amt-10-2923-2017, 2017b.

Dubovik, O., Holben, B. N., and Eck, T. F. et al.: Variability of absorption and optical properties of key aerosol types observed in worldwide locations, J. Atmos. Sci., 59, 590– 608, 2002.Dunion, J. P., and C. S. Velden: The impact of the Saharan air layer on Atlantic tropical cyclone activity, Bull. Am. Meteorol. Soc., 85(3), 353. Meteoro:10.1175/BAMS-85-3-353, 2004.

Engelbrecht, J. P., Moosmüller, H., Pincock, S., Jayanty, R. K. M., Lersch, T., and Casuccio, G.: Technical note: Mineralogical, chemical, morphological, and optical interrelationships of mineral dust re-suspensions, Atmos. Chem. Phys., 16, 10809-10830, https://doi.org/10.5194/acp-16-10809-2016, 2016.Feng, Q., P. Yang, G. W. Kattawar, C. N. Hsu, S.-C. Tsay, and I. Laszlo: Effects of particle nonsphericity and radiation polarization on retrieving dust properties from MODIS observations, J. Aerosol Sci., 40(9), 776–789, doi:10.1016/j.jaerosci.2009.05.001, 2009.

Flores, J. M., Trainic, M., Borrmann, S., and Rudich, Y.: Effective broadband refractive index retrieval by a white light optical particle counter, Phys. Chem. Chem. Phys., 11, 7943–7950, 2009.

Formenti, P., Andreae, M. O., Lange, L., Roberts, G., Cafmeyer, J., Rajta, I., Maenhaut, W., Holben, B. N., Artaxo, P., and Lelieveld, J.: Saharan dust in Brazil and Suriname during the Large-Scale Biosphere–Atmosphere Experiment in Amazonia (LBA) – Cooperative LBA Regional Experiment (CLAIRE) in March 1998, J. Geophys. Res., 106, 14919–14934, https://doi.org/10.1029/2000jd900827, 2001.

829 Formenti, P., Rajot, J. L., Desboeufs, K., Said, F., Grand, N., Chevaillier, S., and Schmechtig, C.: Airborne obser-
830   vations of mineral dust over western Africa in the summer Monsoon season: spatial and vertical variability of
831   physico-chemical and optical properties, Atmos. Chem. Phys., 11, 6387-6410, doi:10.5194/acp-11-6387-2011,
832   2011.

833 Formenti, P., Caquineau, S., Desboeufs, K., Klaver, A., Chevaillier, S., Journet, E., and Rajot, J. L.: Mapping the
834   physicochemical properties of mineral dust in western Africa: mineralogical composition, Atmos. Chem. Phys.,
835   14, 10663–10686, https://doi.org/10.5194/acp-14-10663-2014, 2014a.

836 Formenti, P., Caquineau, S., Chevaillier, S., Klaver, A., Desboeufs, K., Rajot, J. L., Belin, S., and Briois, V.: Domi-
837   nance of goethite over hematite in iron oxides of mineral dust from western Africa: quantitative partitioning by
838   X-ray Absorption Spectroscopy, J. Geophys. Res.-Atmos., 119, 12740–12754,
839   https://doi.org/10.1002/2014JD021668, 2014b.

840 Gasteiger, J., Wiegner, M., Groß, S., Freudenthaler, V., Toledano, C., Tesche, M., and Kandler, K.: Modelling lidar-
841   relevant optical properties of complex mineral dust aerosols, Tellus B, 63, 725–741,
842   https://doi.org/10.1111/j.1600-0889.2011.00559.x, 2011.

843 Ginoux, P., Prospero, J. M., Gill, T. E., Hsu, N. C., and Zhao, M.: Global-scale attribution of anthropogenic and
844   natural dust sources and their emission rates based on MODIS Deep Blue aerosol products, Rev. Geophys.,
845   50, RG3005, doi:10.1029/2012RG000388, 2012.

846 Haywood, J., Francis, P., Osborne, S., Glew, M., Loeb, N., Highwood, E., Tanré, D., Myhre, G., Formenti, P., and
847   Hirst, E.: Radiative properties and direct radiative effect of Saharan dust measured by the C-130 aircraft during
848   SHADE: 1. Solar spectrum, J. Geophys. Res., 108(D18), 8577, doi:10.1029/2002JD002687, 2003.

849 Hess, M., Koepke, P., and Schult, I.: Optical properties of aerosols and clouds: The software package OPAC, Bull.
850   Am. Meteorol. Soc, 79, 831–844, 1998.

851 Highwood, E. J., and Ryder, C. L.: Radiative effects of dust. In Mineral Dust: A Key Player in the Earth System. P.
852   Knippertz, and J.-B.W. Stuut, Eds. Springer, 267-286, doi:10.1007/978-94-017-8978-3_13, 2014.

853 Hsu, N. C., Tsay, S.-C., King, M. D., and Herman, J. R.: Aerosol properties over bright-reflecting source regions,
854   IEEE T. Geosci. Remote Sens., 42, 557–569, 2004.

855 Iwasaka, Y., Shi, G.-Y., Shen, Z., Kim, Y. S., Trochkin, D., Matsuki, A., Zhang, D., Shibata, T., Nagatani, M., and
856   Nakata, H.: Nature of atmospheric aerosols over the desert area in the Asian continent: chemical state and
857   number concentration of particles measured at Dunhuang, China, Water Air Soil Poll., 3, 129–145, 2003

858 Jeong, G. Y., J. Y. Kim, J. Seo, G. M. Kim, H. C. Jin, and Y. Chun: Long-range transport of giant particles in Asian
859   dust identified by physical, mineralogical, and meteorological analysis, Atmos. Chem. Phys., 14(1), 505–521,
860   doi:10.5194/acp-14-505-2014, 2014.

861 Jin, Q., Zang, Z.-L., and Wei, J.: High sensitivity of Indian summer monsoon to Middle East dust absorptive prop-
862   erties, Sci. Rep, 6:30690, doi: 10.1038/srep30690, 2016.

863 Johnson, B. T. and Osborne, S. R.: Physical and optical properties of mineral dust aerosol measured by aircraft
864   during the GERBILS campaign. Q.J.R. Meteorol. Soc., 137: 1117-1130. doi:10.1002/qj.777, 2011.

865 Journet, E., Balkanski, Y., and Harrison, S. P.: A new data set of soil mineralogy for dust-cycle modeling, Atmos.
866   Chem. Phys., 14, 3801-3816, doi:10.5194/acp-14-3801-2014, 2014.

867 Kalashnikova, O. V. and Sokolik, I. N.: Modeling the radiative properties of nonspherical soil-derived mineral aero-
868   sols, J. Quant. Spectrosc. Ra., 87, 137–166, 2004.

869 Kandler, K., Schütz, L., Deutscher, C., Ebert, M., Hofmann, H., Jäckel, S., Jaenicke, R., Knippertz, P., Lieke, K.,
870   Massling, A., Petzold, A., Schladitz, A.,Weinzierl, B.,Wiedensohler, A., Zorn, S., and Weinbruch, S.: Size dis-
871   tribution, mass concentration, chemical and mineralogical composition and derived optical parameters of the
872   boundary layer aerosol at Tinfou, Morocco, during SAMUM 2006, Tellus B, 61, 32–50, doi:10.1111/j.1600-
873   0889.2008.00385.x, 2009.

874 Karickhoff, S.W. and Bailey, G.W. 1973. Optical absorption spectra of clay minerals. Clay Clay Miner., 21, 59–
875   70.Kaufman, Y. J.: Satellite sensing of aerosol absorption, J. Geophys. Res., 92, 4307–4317, 1987.

876 Kaufman, Y. J., Tanr'e, D., Dubovik, O., Karnieli, A., and Remer, L. A.: Absorption of sunlight by dust as inferred
877   from satellite and ground-based remote sensing, Geophys. Res. Lett., 28, 1479–1482, 2001.

878 Koepke, P., Gasteiger, J., and Hess, M.: Technical Note: Optical properties of desert aerosol with non-spherical
879   mineral particles: data incorporated to OPAC, Atmos. Chem. Phys., 15, 5947-5956, https://doi.org/10.5194/acp-
880   15-5947-2015, 2015.

881   Kok, J.F., D.A. Ridley, Q. Zhou, R.L. Miller, C. Zhao, C.L. Heald, D.S. Ward, S. Albani, and K. Haustein: Smaller
882   desert dust cooling effect estimated from analysis of dust size and abundance. Nature Geosci., 10, no. 4, 274-
883   278, doi:10.1038/ngeo2912, 2017.

884   Konaré, A., Zakey, A. S., Solmon, F., Giorgi, F., Rauscher, S., Ibrah, S., and Bi, X.: A regional climate modeling
885   study of the effect of desert dust on the West African monsoon, J. Geophys. Res., 113, D12206,
886   doi:10.1029/2007JD009322, 2008.

887   Koven, C.D., and Fung, I.: Inferring dust composition from wavelength-dependent absorption in Aerosol Robotic
888   Network (AERONET) data. J Geophys Res 111, D14205. doi:10.1029/2005JD006678, 2006.

889   Lafon, S., Sokolik, I. N., Rajot, J. L., Caquineau, S., and Gaudichet, A.: Characterization of iron oxides in mineral
890   dust aerosols: Implications for light absorption, J. Geophys. Res., 111, D21207, doi:10.1029/2005jd007016, 2006.

891   Liao, H. and Seinfeld, J. H.: Radiative forcing by mineral dust aerosols: sensitivity to key variables, J. Geophys.
892   Res., 103(D24), 31 637–31 646, doi:10.1029/1998JD200036, 1998.

893   Lide, D. R.: CRC Handbook of Chemistry and Physics 1991–1992, CRC Press, Boca Raton, Florida, 1992.

894   Linke, C., Möhler, O., Veres, A., Mohácsi, A., Bozóki, Z., Szabó, G., and Schnaiter, M., Optical properties and
895   mineralogical composition of different Saharan mineral dust samples: a laboratory study, Atmos. Chem. Phys.,
896   6, 3315–3323, 2006.

897   Lu, H., Wei, W., Liu, M., Wu, X., Mou, S., and Han, Q.: Quantification and semi-quantification of iron-oxide minerals
898   in aerosol particles in the hinterland of Taklimakan Desert, Scientia Geographica Sinica, 31, 969–975, 2011.

899   Maring, H., Savoie, D. L., Izaguirre, M. A., McCormick, C., Arimoto, R., Prospero, J. M., and Pilinis, C.: Aerosol
900   physical and optical properties and their relationship to aerosol composition in the free troposphere at izana,
901   tenerife, canary islands, during July 1995, J. Geophys. Res.-Atmos., 105, 14677–14700, 2000.

902   Maring, H., Savoie, D. L., Izaguirre, M. A., Custals, L., and Reid, J. S.: Mineral dust aerosol size distribution change
903   during atmospheric transport, J. Geophys. Res., 108, 8592, doi:10.1029/2002jd002536, 2003.

904   McConnell, C. L., Highwood, E. J., Coe, H., Formenti, P., Anderson, B., Osborne, S., Nava, S., Desboeufs, K.,
905   Chen, G., and Harrison, M. A. J.: Seasonal variations of the physical and optical characteristics of Saharan
906   dust: Results from the Dust Outflow and Deposition to the Ocean (DODO) experiment, J. Geophys. Res., 113,
907   D14S05, doi:10.1029/2007jd009606, 2008.

908   McConnell, C. L., Formenti, P., Highwood, E. J., and Harrison, M. A. J.: Using aircraft measurements to determine
909   the refractive index of Saharan dust during the DODO Experiments, Atmos. Chem. Phys., 10, 3081–3098,
910   doi:10.5194/acp-10-3081-2010, 2010.

911   Miller, R. L., I. Tegen, and J. Perlwitz: Surface radiative forcing by soil dust aerosols and the hydrologic cycle, J.
912   Geophys. Res., 109, D04203, doi:10.1029/2003JD004085, 2004.

913   Miller, R. L., Knippertz, P., Pérez García-Pando, C., Perlwitz, J. P., and Tegen, I.: Impact of dust radiative forcing
914   upon climate. In Mineral Dust: A Key Player in the Earth System. P. Knippertz, and J.-B.W. Stuut, Eds. Springer,
915   327-357, doi:10.1007/978-94-017-8978-3_13, 2014.

916   Mishchenko, M., A. Lacis, B. Carlson, and L. Travis: Nonsphericity of dust-like tropospheric aerosols—Implications
917   for aerosol remotesensing and climate modeling, Geophys. Res. Lett., 22(9), 1077–1080, 1995.

918   Moosmüller, H., Engelbrecht, J. P., Skiba, M., Frey, G., Chakrabarty, R.K., and Arnott, W.P., Single scattering
919   albedo of fine mineral dust aerosols controlled by iron concentration, J. Geophys. Res., 117, D11210,
920   doi:10.1029/2011JD016909, 2012.

921   Müller, T., Schladitz, A., Massling, A., Kaaden, N., Kandler, K., and coauthors: Spectral absorption coefficients and
922   imaginary parts of refractive indices of Saharan dust during SAMUM-1. Tellus 61B, 79–95, 2009.

923   Muller, T., Schladitz, A., Kandler, K., and Wiedensohler, A.: Spectral particle absorption coefficients, single scat-
924   tering albedos and imaginary parts of refractive indices from ground based in situ measurements at Cape Verde
925   Island during SAMUM-2, Tellus B, 63, 573–588, doi:10.1111/j.1600-0889.2011.00572.x, 2011.

926   Myhre, G. and Stordal, F.: Global sensitivity experiments of the radiative forcing due to mineral aerosols, J. Ge-
927   ophys. Res., 106(D16), 18 193–18 204, doi:10.1029/2000JD900536, 2001.

928   Nickovic, S., Vukovic, A., Vujadinovic, M., Djurdjevic, V., and Pejanovic, G.: Technical Note: High-resolution min-
929   eralogical database of dust-productive soils for atmospheric dust modeling, Atmos. Chem. Phys., 12, 845–855,
930   doi:10.5194/acp-12-845-2012, 2012.

931   Nousiainen, T. and Kandler, K.: Light scattering by atmospheric mineral dust particles, in: Light Scattering Reviews
932   9, edited by: Kokhanovsky, A. A., Springer Praxis Books, Springer, Berlin, Heidelberg, 3–52, doi:10.1007/978-
933   3-642-37985-7, 2015. 16863, 16864, 16866

934   Okada, K., Heintzenberg, J., Kai, K., Qin, Y., 2001. Shape of atmospheric mineral particles collected in three Chi-
935   nese arid-regions. Geophys. Res. Lett. 28 (16), 3123–3126

936   Osborne, S.R., Johnson, B.T., Haywood, J.M., Baran, A.J., Harrison, M.A.J., and McConnell, C.L.: Physical and
937   optical properties of mineral dust aerosol during the Dust and Biomass-burning Experiment, J. Geophys. Res.,
938   113, D00C03, doi:10.1029/2007jd009551, 2008.

939   Otto, S., Bierwirth, E., Weinzierl, B., Kandler, K., Esselborn, M., Tesche, M., Schladitz, A.,Wendisch, M., and Tra-
940   utmann, T.: Solar radiative effects of a Saharan dust plume observed during SAMUM assuming spheroidal
941   model particles, Tellus B, 61, 270–296, doi:10.1111/j.1600-0889.2008.00389.x, 2009.

942   Patterson, E.M., Filette, D. A., and Stockton, B. H.: Complex index of refraction between 300 and 700 nm for
943   Saharan aerosols, J. Geophys. Res., 82, 3153–3160, 1977.

944   Perlwitz, J. P., Pérez García-Pando, C., and Miller, R. L.: Predicting the mineral composition of dust aerosols –
945   Part 1: Representing key processes, Atmos. Chem. Phys., 15, 11593-11627, https://doi.org/10.5194/acp-15-
946   11593-2015, 2015a.

947   Perlwitz, J. P., Pérez García-Pando, C., and Miller, R. L.: Predicting the mineral composition of dust aerosols –
948   Part 2: Model evaluation and identification of key processes with observations, Atmos. Chem. Phys., 15, 11629-
949   11652, https://doi.org/10.5194/acp-15-11629-2015, 2015b.

950   Petzold, A., Schloesser, H., Sheridan, P. J., Arnott, W. P., Ogren, J. A., and Virkkula, A.: Evaluation of Multi-angle
951   Absorption Photometry for Measuring Aerosol Light Absorption, Aerosol Sci. Technol., 39, 40–51, 2005.

952   Petzold, A., Rasp, K., Weinzierl, B., Esselborn, M., Hamburger, T., Dornbrack, A., Kandler, K., Schutz, L., Knip-
953   pertz, P., Fiebig, M., Virkkula, A., Saharan dust absorption and refractive index from aircraft-based observations
954   during SAMUM 2006, Tellus B 61: 118–130, 2009.

955   Petzold, A., Onasch, T., Kebabian, P., and Freedman, A.: Intercomparison of a Cavity Attenuated Phase Shift-
956   based extinction monitor (CAPS PMex) with an integrating nephelometer and a filter-based absorption monitor,
957   Atmos. Meas. Tech., 6, 1141-1151, doi:10.5194/amt-6-1141-2013, 2013.Räisänen, P., P. Haapanala, C. E.
958   Chung, M. Kahnert, R. Makkonen, J. Tonttila, and T. Nousiainen: Impact of dust particle non-sphericity on
959   climate simulations, Q. J. R. Meteorol. Soc., 139, 2222–2232, doi:10.1002/qj.2084, 2012.

960   Rajot, J. L., Formenti, P., Alfaro, S., Desboeufs, K., Chevaillier, S., Chatenet, B., Gaudichet, A., Journet, E., Marti-
961   corena, B., Triquet, S., Maman, A., Mouget, N., and Zakou, A.: AMMA dust experiment: an overview of meas-
962   urements performed during the dry season special observation period (SOP0) at the Banizoumbou (Niger)
963   supersite, J. Geophys. Res., 113, D00C14, doi:10.1029/2008jd009906, 2008.

964   Redmond, H. E., Dial, K. D., and Thompson, J.E.: Light scattering and absorption by wind-blown dust: theory,
965   measurement and recent data, Aeolian Res., 2, 5-26, 2010.

966   Reid, E. A., Reid, J. S., Meier, M. M., Dunlap, M. R., Cliff, S. S., Broumas, A., Perry, K., and Maring, H.: Charac-
967   terization of African dust transported to Puerto Rico by individual particle and size segregated bulk analysis, J.
968   Geophys. Res., 108, 8591, doi:10.1029/2002jd002935, 2003.

969   Ridley, D. A., Heald, C. L., Kok, J. F., and Zhao, C.: An observationally constrained estimate of global dust aerosol
970   optical depth, Atmos. Chem. Phys., 16, 15097-15117, https://doi.org/10.5194/acp-16-15097-2016, 2016.

971   Rocha-Lima, A., Martins, J. V., Remer, L. A., Todd, M., Marsham, J. H., Engelstaedter, S., Ryder, C. L., Cavazos-
972   Guerra, C., Artaxo, P., Colarco, P., and Washington, R.: A detailed characterization of the Saharan dust col-
973   lected during the Fennec campaign in 2011: in situ ground-based and laboratory measurements, Atmos. Chem.
974   Phys., 18, 1023-1043, https://doi.org/10.5194/acp-18-1023-2018, 2018.

975   Ryder, C. L., Highwood, E. J., Rosenberg, P. D., Trembath, J, Brooke, J. K., Bart, M., Dean, A., Crosier, J., Dorsey,
976   J., Brindley, H., Banks, J., Marsham, J. H., McQuaid, J. B., Sodemann, H., and Washington, R.: Optical prop-
977   erties of Saharan dust aerosol and contribution from the coarse mode as measured during the Fennec 2011
978   aircraft campaign, Atmos. Chem. Phys., 13, 303-325, doi:10.5194/acp-13-303-2013, 2013a.

979   Ryder, C. L., Highwood, E. J., Lai, T. M., Sodemann, H., and Marsham J. H.: Impact of atmospheric transport on
980   the evolution of microphysical and optical properties of Saharan dust, Geophys. Res. Lett., 40, 2433–2438, doi:
981   10.1002/grl.50482, 2013b.

982   Samset, B. H., Stjern, C. W., Andrews, E., Kahn, R. A., Myhre, G., Schulz, M., and Schuster, G. L.: Aerosol Ab-
983   sorption: Progress Towards Global and Regional Constraints, Curr. Clim. Change Rep., 4, 65–83, 2018.

984   Saturno, J., Pöhlker, C., Massabo, D., Brito, J., Carbone, S., Cheng, Y. F., Chi, X. G., Ditas, F., de Angelis, I. H.,
985   Moran-Zuloaga, D., Pohlker, M. L., Rizzo, L. V., Walter, D., Wang, Q. Q., Artaxo, P., Prati, P., and Andreae, M.
986   O., Comparison of different Aethalometer correction schemes and a reference multi-wavelength absorption
987   technique for ambient aerosol data: Atmos. Meas. Tech., 10, 2837-2850, doi:10.5194/amt-10-2837-2017, 2017.

Scanza, R. A., Mahowald, N., Ghan, S., Zender, C. S., Kok, J. F., Liu, X., Zhang, Y., and Albani, S.: Modeling dust as component minerals in the Community Atmosphere Model: development of framework and impact on radiative forcing, Atmos. Chem. Phys., 15, 537-561, doi:10.5194/acp-15-537-2015, 2015.

Scheuvens, D., Schütz, L., Kandler, K., Ebert, M., and Weinbruch, S.: Bulk composition of northern African dust and its source sediments – A compilation, Earth-Sci. Rev., 116, 170–194, https://doi.org/10.1016/j.earsci-rev.2012.08.005, 2013.

Schladitz, A., Müller, T., Kaaden, N., Massling, A., Kandler, K., Ebert, M., Weinbruch, S., Deutscher, C., and Wiedensohler, A.: In situ measurements of optical properties at Tinfou (Morocco) during the Saharan Mineral Dust Experiment SAMUM 2006, Tellus B, 61, 64–78, doi:10.1111/j.1600-0889.2008.00397.x, 2009.

Shen, Z., Cao, J., Zhang, X., Arimoto, R., Ji, J., Balsam, W., Wang, Y., Zhang, R., and Li, X.: Spectroscopic analysis of iron-oxide minerals in aerosol particles from northern China, Sci. Total Environ., 367, 899–907, 2006.

Shettle, E. P., and Fenn, R.W.: Models for the Aerosols of the Lower Atmosphere and the Effects of Humidity Variations on Their Optical Properties, AFGL-TR-79-0214, ADA085951, 1979.

Shin, S.-K., Tesche, M., Kim, K., Kezoudi, M., Tatarov, B., Müller, D., and Noh, Y.: On the spectral depolarisation and lidar ratio of mineral dust provided in the AERONET version 3 inversion product, Atmos. Chem. Phys., 18, 12735-12746, https://doi.org/10.5194/acp-18-12735-2018, 2018.

Sinyuk, A., Torres, O., and Dubovik, O., Combined use of satellite and surface observations to infer the imaginary part of refractive index of Saharan dust, Geophys. Res. Lett., 30(2), 1081, doi:10.1029/2002GL016189, 2003.

Sokolik, I., and Toon, O.: Incorporation of mineralogical composition into models of the radiative properties of mineral aerosol from UV to IR wavelengths, J. Geophys. Res., 104(D8), 9423-9444, 1999.

Sokolik, I.N., Andronova, A.V., and Jonhson, T.C.: Complex refractive index of atmospheric dust aerosols, Atmos. Environ., 16, 2495–2502, 1993.

Solmon, F., Mallet, M., Elguindi, N., Giorgi, F., Zakey, A. and Konaré, A.: Dust aerosol impact on regional precipitation over western Africa, mechanisms and sensitivity to absorption properties, Geophys. Res. Lett., 35, L24705, doi:10.1029/2008GL035900, 2008.

Stegmann, P. G., Yang, P., A regional, size-dependent, and causal effective medium model for Asian and Saharan mineral dust refractive index spectra, J. Aer. Sci., 114, 327-341, 2017.

Strong, J. D. O., Vecchi, G. A., & Ginoux, P.: The climatological effect of Saharan dust on global tropical cyclones in a fully coupled GCM. Journal of Geophysical Research: Atmospheres, 123, 5538–5559. https://doi-org.insu.bib.cnrs.fr/10.1029/2017JD027808, 2018

Su, L., and Toon O.B.: Saharan and Asian dust: similarities and differences determined by CALIPSO, AERONET, and a coupled climate-aerosol microphysical model, Atmos. Chem. Phys.; 11, 3263–3280, 2011.

Todd, M. C., R. Washington, J. V. Martins, O. Dubovik, G. Lizcano, S. M'Bainayel, and S. Engelstaedter, Mineral dust emission from the Bodélé Depression, northern Chad, during BoDEx 2005, J. Geophys. Res., 112, D06207, doi:10.1029/2006JD007170, 2007.

Toon, O. B., Pollack, J. B., and Khare, B. N.: The optical constants of several atmospheric aerosol species: ammonium sulphate, aluminum oxide, and sodium chloride, J. Geophys. Res., 81, 5733–5748, 1976.

Uno, I., K. Eguchi, K. Yumimoto, T. Takemura, A. Shimizu, M. Uematsu, Z. Liu, Z. Wang, Y. Hara, and N. Sugimoto, Asian dust transported one full circuit around the globe, Nat. Geosci,2, 557–560, doi:10.1038/ngeo583, 2009.

Vinoj, V. et al. Short-term modulation of Indian summer monsoon rainfall by West Asian dust. Nature Geoscience 7, 308–313, 2014.

Volz, F. E.: Longwave refractive index of atmospheric aerosol substances, Appl. Optics, 11, 755-759, 1972.

Wang, J., Doussin, J. F., Perrier, S., Perraudin, E., Katrib, Y., Pangui, E., and Picquet-Varrault, B.: Design of a new multi-phase experimental simulation chamber for atmospheric photosmog, aerosol and cloud chemistry research, Atmos. Meas. Tech., 4, 2465–2494, 2011.

Wagner, R., Ajtai, T., Kandler, K., Lieke, K., Linke, C., Müller, T., Schnaiter, M., and Vragel, M.: Complex refractive indices of Saharan dust samples at visible and near UV wavelengths: a laboratory study, Atmos. Chem. Phys., 12, 2491-2512, doi:10.5194/acp-12-2491-2012, 2012.

Weingartner, E., Saathoff, H., Schnaiter, M., Streit, N., Bitnar, B., and Baltensperger, U.: Absorption of light by soot particles: determination of the absorption coefficient by means of aethalometers, J. Aerosol Sci., 34, 1445–1463, 2003.

1039 Weinzierl, B., Petzold, A., Esselborn, M., Wirth, M., Rasp, K., Kandler, K., Schutz, L., Koepke, P., and Fiebig, M.:
1040   Airborne measurements of dust layer properties, particle size distribution and mixing state of Saharan dust
1041   during SAMUM 2006, Tellus, 61B, 96-117, doi:10.1111/j.1600-0889.2008.00392.x, 2009.

1042 Weinzierl, B., Sauer, D., Esselborn, M., Petzold, A., Veira, A., Rose, M., Mund, S.,Wirth, M., Ansmann, A., Tesche,
1043   M., Gross, S., and Freudenthaler, V.: Microphysical and optical properties of dust and tropical biomass burning
1044   aerosol layers in the Cape Verde region-an overview of the airborne in situ and lidar measurements during
1045   SAMUM-2, Tellus B, 63, 589–618, doi:10.1111/j.1600-0889.2011.00566.x, 2011.

1046 Yi, B., C. N. Hsu, P. Yang, and S.-C. Tsay: Radiative transfer simulation of dust-like aerosols uncertainties from
1047   particle shape and refractive index, J. Aerosol Sci., 42(10), 631–644, doi:10.1016/j.jaerosci.2011.06.008, 2011.

1048 Yoshida, M. and Murakami, H.: Dust absorption averaged over the Sahara inferred from moderate resolution im-
1049   aging spectroradiometer data, Appl. Opt., 47, 1995–2003, 2008.

1050 Yoshioka, M., Mahowald, N.M., Conley, A.J., Collins, W.D., Fillmore, D.W., Zender, C.S., and Coleman, D.B.: Im-
1051   pact of desert dust radiative forcing on sahel precipitation: Relative importance of dust compared to sea surface
1052   temperature variations, vegetation changes, and greenhouse gas warming, J. Clim., 20, 1445– 1467, 2007.

1053
1054
1055
1056
1057
1058
1059
1060
1061
1062
1063
1064
1065
1066
1067
1068
1069
1070
1071
1072
1073
1074
1075
1076
1077
1078
1079
1080
1081
1082
1083
1084
1085
1086

Table 1. Measured and retrieved quantities and their estimated uncertainties. For further details, refer to Sect. 2, as well DB17 and C17.

Parameter		Time resolution	Uncertainty	Uncertainty calculation	Comments
Optical SW	Scattering coefficient at 450, 550, and 700 nm, $\beta_{sca}(\lambda)$	*10–min data*	5–12%	Quadratic combination of photon counting and gas calibration uncertainty (5%), angular corrections uncertainty (<5%) and standard deviation over 10–min intervals (2-10%).	The uncertainty on $\beta_{sca}(\lambda)$ usually decreases with increasing dust residence time in the chamber as a result of the reduction of the coarse component.
	Absorption coefficient at 370, 470, 520, 590, 660, 880, and 950 nm, $\beta_{abs}(\lambda)$	*10–min data*	22–30% at 370 nm 23–87% at 950 nm	Error propagation formula[1] on Eq. (2) considering the uncertainties on $\beta_{ATT}(\lambda)$ from 10–min fitting procedure (error propagation formula[1] on Eq. 1, ~20%), and uncertainties on $\alpha(\lambda)$ (1%), $\beta_{sca}(\lambda)$ (5–12%), C_{ref} (10%), and R (1–10%).	
	Extinction coefficient, $\beta_{ext}(\lambda) = \beta_{sca}(\lambda) + \beta_{abs}(\lambda)$	*10–min data*	~25%	Sum of $\beta_{sca}(\lambda)$ and $\beta_{abs}(\lambda)$ uncertainties	
	Single Scattering Albedo, SSA (λ) = $\beta_{sca}(\lambda) / (\beta_{sca}(\lambda) + \beta_{abs}(\lambda))$	*10–min data*	9–12%	Error propagation formula[1] considering single uncertainties on β_{sca} and β_{abs}.	
	Single Scattering Albedo, SSA (λ) = $(1+1/m(\lambda))^{-1}$	*Experiment averaged*	1–12% at 370 nm 1–3% at 950 nm	Error propagation formula[1] on Eq. (6) considering the uncertainty on $m(\lambda)$, i.e., the slope of the linear fit between β_{sca} and β_{abs} over the whole duration of each experiment.	
	Complex refractive index (n-ik)	*10–min data*	<5% for n <50% for k	Deviations of the values of n and k retrieved in the sensitivity study (see Sect. 3.2) with respect to those obtained in the first inversions were assumed to correspond to the one standard deviation uncertainty to 10–min retrieved values.	
	Complex refractive index (n-ik)	*Experiment averaged*	<8% for n 13–75 % for k	Quadratic combination of the standard deviation of n and k over the experiment and the deviation on the experiment–averaged values between those obtained from central inversions and inversions using input data ± their uncertainty.	
Size distribution	SMPS geometrical diameter (D_g), $D_g = D_m / \chi$	–	~6%	Error propagation formula[1] considering the uncertainty on the estimated shape factor χ (~6%)	The electrical mobility to geometrical diameter conversion was performed by assuming for dust a dynamic shape factor of 1.75 ± 0.10, as determined by SMPS–SkyGrimm comparison

					in their overlapping range (see DB17)
	SkyGrimm geometrical diameter (D_g)	–	<15.2%	Standard deviation of the D_g values obtained for different refractive indices values used in the optical to geometrical conversion	The conversion of optical to geometrical diameters for the SkyGrimm and the WELAS was performed by Mie calculations by varying the dust refractive index in the range 1.47–1.53 for the real part and 0.001–0.005 for the imaginary part. Then D_g is set at the mean ± 1 standard deviation of the values obtained for the different values of n and k (see DB17). Refractive index is assumed to be constant with particle size and wavelength–independent.
	WELAS geometrical diameter (D_g)	–	<7%	The same as for the SkyGrimm	
	$(dN/dlogD)_{SWoptics}$	*10–min data*	~20-90%	Error propagation formula[1] considering the $dN/dlogD_g$ st. dev. over 10-min and the uncertainty on particle loss function along sampling tubes $L(D_g)$ (~50% at 2 µm, ~10% at 8 µm)	The uncertainty of $L(D_g)$ was estimated with a sensitivity study by varying the values of the input parameters to the Particle Loss Calculator software within their uncertainties (see DB17)
	$D_{eff,fine}$	*10–min data*	<5%	Deviation obtained by repeating the calculations by using the size distribution ± its uncertainty.	
	$D_{eff,coarse}$	*10–min data*	5–40%		
Mineralogical composition	Elemental iron mass concentration ($MC_{Fe\%}$)	*Experiment averaged*	10%	Uncertainties calculated as discussed in DB17 and C17	
	Iron oxides mass concentration ($MC_{Fe-ox\%}$)	*Experiment averaged*	15%		
	Goethite mass concentration ($MC_{Goet\%}$)	*Experiment averaged*	<10%		
	Hematite mass concentration ($MC_{Hem\%}$)	*Experiment averaged*	<10%		

1090   [1] $\sigma_f = \sqrt{\sum_{i=1}^{n}\left(\dfrac{\partial f}{\partial x_i}\sigma_{x_i}\right)^2}$

1091
1092
1093
1094
1095
1096
1097
1098
1099
1100
1101
1102
1103
1104
1105

1106 **Table 2.** Summary of information on the soil samples and sediments used in this study.
1107
1108

Geographical area	Sample	Coordinates	Desert area
Northern Africa – Sahara	Tunisia	33.02°N, 10.67°E	Maouna
	Morocco	31.97°N, 3.28°W	east of Ksar Sahli
	Libya	27.01°N, 14.50°E	Sebha
	Algeria	23.95°N, 5.47°E	Ti-n-Tekraouit
	Mauritania	20.16°N, 12.33°W	east of Aouinet Nchir
Sahel	Niger	13.52°N, 2.63°E	Banizoumbou
	Mali	17.62°N, 4.29°W	Dar el Beida
	Bodélé	17.23°N, 19.03°E	Bodélé depression
Eastern Africa and the Middle East	Ethiopia	7.50°N, 38.65°E	Lake Shala National Park
	Saudi Arabia	27.49°N, 41.98°E	Nefud
	Kuwait	29.42°N, 47.69°E	Kuwaiti
Eastern Asia	Gobi	39.43°N, 105.67°E	Gobi
	Taklimakan	41.83°N, 85.88°E	Taklimakan
North America	Arizona	33.15 °N, 112.08°W	Sonoran
South America	Atacama	23.72°S, 70.40°W	Atacama
	Patagonia	50.26°S, 71.50°W	Patagonia
Southern Africa	Namib-1	21.24°S, 14.99°E	Namib
	Namib-2	19.00°S, 13.00°E	Namib
Australia	Australia	31.33°S, 140.33°E	Strzelecki

1109
1110

1111 **Table 3**. Chemical characterization of the dust aerosols in the $PM_{10.6}$ size fraction. Column 3 shows
1112 $MC_{Fe\%}$, the fractional mass of elemental iron with respect to the total dust mass concentration (±10 %),
1113 and column 4 reports $MC_{Fe-ox\%}$, the mass fraction of iron oxides with respect to the total dust mass
1114 concentration (±15 %) and its speciation in hematite $MC_{Hem\%}$ and goethite $MC_{Goeth\%}$ ($<\pm10\%$). The iron
1115 oxide measurements were not made on the Taklimakan sample. Mean values and standard deviations
1116 based on single sample data are reported for the full dataset.

1117

Geographical area	Sample	$MC_{Fe\%}$	$MC_{Fe-ox\%}$	$MC_{Hem\%}$	$MC_{Goet\%}$
Northern Africa – Sahara	Tunisia	4.1	2.2	1.2	1.1
	Morocco	3.6	1.4	0.4	1.0
	Libya	5.2	3.1	0.9	2.2
	Algeria	6.6	2.7	1.4	1.4
	Mauritania	8.1	3.3	3.3	0.0
Sahel	Niger	6.1	5.8	2.3	3.5
	Mali	6.6	3.7	2.0	1.7
	Bodélé	4.1	0.7	0.7	0.0
Eastern Africa and the Middle East	Ethiopia	6.8	2.0	2.0	0.0
	Saudi Arabia	3.8	2.6	1.8	0.8
	Kuwait	5.0	1.5	1.5	0.0
Eastern Asia	Gobi	4.8	0.9	0.9	0.0
	Taklimakan	5.8	–	–	–
North America	Arizona	5.3	1.5	1.5	0.0
South America	Atacama	4.7	1.6	1.6	0.0
	Patagonia	5.1	1.5	0.9	0.6
Southern Africa	Namib-1	2.4	1.1	0.8	0.3
	Namib-2	10.6	4.8	4.8	0.0
Australia	Australia	7.2	3.6	3.6	0.0
Full dataset mean (st. dev.)		**5.6 (1.9)**	**2.4 (1.4)**	**1.8 (1.1)**	**0.7 (1.0)**

1118

1119 **Table 4.** Real (n) and imaginary (k) parts of the refractive index estimated for the nineteen analysed
1120 dust samples and mean values calculated for the eight regions and for the full dataset. Data for single
1121 soils are reported as experiment–averaged values and their uncertainty is calculated as indicated in
1122 Table 1. Mean values and standard deviations at each wavelength based on single sample data are
1123 reported for the eight regions and the full dataset. The median and 10% and 90% percentile values are
1124 also reported for the full dataset. For North America and Australia, for which only one dust sample was
1125 analysed, the reported data correspond to the single sample available from these regions. For the real
1126 part, the average over the whole shortwave range (nSW) is indicated.
1127

Sample/Region	nSW 037–0.95 µm	σnSW 037–0.95 µm	k 0.37 µm	k 0.47 µm	k 0.52 µm	k 0.59 µm	k 0.66 µm	k 0.88 µm	k 0.95 µm	σk 0.37 µm	σk 0.47 µm	σk 0.52 µm	σk 0.59 µm	σk 0.66 µm	σk 0.88 µm	σk 0.95 µm
Tunisia	1.51	0.06	0.0045	0.0035	0.0026	0.0018	0.0015	0.0013	0.0012	0.0030	0.0026	0.0018	0.0012	0.0010	0.0008	0.0007
Morocco	1.49	0.03	0.0023	0.0016	0.0012	0.0008	0.0007	0.0006	0.0007	0.0006	0.0004	0.0003	0.0002	0.0002	0.0002	0.0002
Lybia	1.5	0.04	0.0029	0.0019	0.0014	0.0007	0.0006	0.0007	0.0007	0.0006	0.0004	0.0002	0.0001	0.0002	0.0002	0.0002
Algeria	1.52	0.04	0.0025	0.0016	0.0012	0.0007	0.0005	0.0006	0.0006	0.0010	0.0006	0.0004	0.0003	0.0003	0.0003	0.0003
Mauritania	1.5	0.03	0.0043	0.0033	0.0026	0.0014	0.0013	0.0010	0.0010	0.0010	0.0009	0.0008	0.0003	0.0003	0.0004	0.0003
Northern Africa – Sahara (mean and st. dev.)	1.51	0.03	0.0033	0.0024	0.0018	0.0011	0.0009	0.0008	0.0008	0.0010	0.0010	0.0007	0.0005	0.0004	0.0003	0.0003
Niger	1.51	0.04	0.0088	0.0061	0.0048	0.0034	0.0031	0.0028	0.0021	0.0043	0.0031	0.0023	0.0018	0.0015	0.0010	0.0013
Mali	1.52	0.05	0.0048	0.0038	0.0030	0.0023	0.0024	0.0021	0.0021	0.0008	0.0006	0.0004	0.0003	0.0003	0.0003	0.0003
Bodélé	1.49	0.03	0.0011	0.0007	0.0006	0.0004	0.0004	0.0003	0.0003	0.0006	0.0004	0.0003	0.0002	0.0002	0.0001	0.0001
Sahel (mean and st. dev.)	1.51	0.03	0.0049	0.0035	0.0028	0.0020	0.0020	0.0017	0.0015	0.0038	0.0027	0.0021	0.0015	0.0014	0.0013	0.0011
Ethiopia	1.55	0.06	0.0026	0.0020	0.0016	0.0013	0.0011	0.0007	0.0006	0.0009	0.0008	0.0007	0.0005	0.0004	0.0002	0.0002
Saudi Arabia	1.54	0.06	0.0028	0.0021	0.0015	0.0007	0.0006	0.0006	0.0006	0.0006	0.0005	0.0004	0.0002	0.0001	0.0001	0.0001
Kuwait	1.50	0.04	0.0016	0.0010	0.0008	0.0006	0.0005	0.0005	0.0004	0.0005	0.0003	0.0003	0.0002	0.0002	0.0003	0.0002
Eastern Africa and the Middle East (mean and st. dev.)	1.53	0.05	0.0023	0.0017	0.0013	0.0009	0.0007	0.0006	0.0005	0.0007	0.0006	0.0005	0.0004	0.0003	0.0001	0.0001
Gobi	1.48	0.05	0.0041	0.0025	0.0018	0.0012	0.0011	0.0012	0.0012	0.0017	0.0009	0.0006	0.0004	0.0004	0.0005	0.0005
Taklimakan	1.54	0.07	0.0018	0.0012	0.0009	0.0006	0.0005	0.0005	0.0005	0.0008	0.0005	0.0004	0.0002	0.0002	0.0002	0.0002
Eastern Asia (mean and st. dev.)	1.51	0.05	0.0030	0.0019	0.0014	0.0009	0.0008	0.0008	0.0009	0.0016	0.0009	0.0006	0.0005	0.0005	0.0005	0.0005
Arizona	1.51	0.05	0.0011	0.0009	0.0007	0.0005	0.0005	0.0005	0.0004	0.0005	0.0004	0.0003	0.0002	0.0002	0.0002	0.0002
North America (mean and st. dev.)	1.51	0.05	0.0011	0.0009	0.0007	0.0005	0.0005	0.0005	0.0004	0.0005	0.0004	0.0003	0.0002	0.0002	0.0002	0.0002
Atacama	1.54	0.07	0.0016	0.0015	0.0012	0.0008	0.0006	0.0006	0.0006	0.0005	0.0004	0.0003	0.0002	0.0002	0.0002	0.0002
Patagonia	1.53	0.07	0.0024	0.0016	0.0011	0.0009	0.0006	0.0007	0.0006	0.0008	0.0005	0.0003	0.0003	0.0003	0.0003	0.0002
South America (mean and st. dev.)	1.54	0.06	0.0020	0.0015	0.0011	0.0008	0.0006	0.0007	0.0006	0.0006	0.0001	0.0001	0.0001	0.0000	0.0001	0.0000
Namib-1	1.53	0.06	0.0012	0.0009	0.0006	0.0004	0.0003	0.0004	0.0004	0.0006	0.0004	0.0003	0.0002	0.0001	0.0002	0.0001
Namib-2	1.55	0.07	0.0072	0.0054	0.0044	0.0025	0.0018	0.0014	0.0014	0.0027	0.0019	0.0016	0.0009	0.0007	0.0006	0.0006
Southern Africa (mean and st. dev.)	1.54	0.06	0.0042	0.0031	0.0025	0.0014	0.0011	0.0009	0.0009	0.0042	0.0032	0.0027	0.0015	0.0010	0.0007	0.0007
Australia	1.54	0.06	0.0058	0.0042	0.0033	0.0017	0.0013	0.0013	0.0012	0.0022	0.0011	0.0010	0.0006	0.0006	0.0004	0.0003
Australia (mean and st. dev.)	1.54	0.06	0.0058	0.0042	0.0033	0.0017	0.0013	0.0013	0.0012	0.0022	0.0011	0.0010	0.0006	0.0006	0.0004	0.0003
Full dataset (mean and st. dev.)	1.52	0.04	0.0033	0.0024	0.0018	0.0012	0.0010	0.0009	0.0009	0.0021	0.0016	0.0013	0.0008	0.0007	0.0006	0.0005
Full dataset median	1.52		0.0026	0.0019	0.0014	0.0008	0.0006	0.0007	0.0006							
Full dataset 10% percentile	1.49		0.0012	0.0009	0.0007	0.0005	0.0004	0.0004	0.0004							
Full dataset 90% percentile	1.54		0.0061	0.0044	0.0035	0.0023	0.0019	0.0015	0.0015							

1128

1129 **Table 5.** As in Table 4 for the single scattering albedo (SSA) data.

Sample/Region	SSA							σ_SSA						
	0.37 µm	0.47 µm	0.52 µm	0.59 µm	0.66 µm	0.88 µm	0.95 µm	0.37 µm	0.47 µm	0.52 µm	0.59 µm	0.66 µm	0.88 µm	0.95 µm
Tunisia	0.85	0.90	0.93	0.95	0.95	0.97	0.97	0.03	0.02	0.02	0.01	0.01	0.01	0.01
Morocco	0.92	0.95	0.96	0.98	0.98	0.98	0.99	0.01	0.01	0.01	0.00	0.00	0.00	0.00
Lybia	0.89	0.93	0.95	0.98	0.98	0.98	0.98	0.02	0.01	0.01	0.00	0.00	0.00	0.00
Algeria	0.87	0.92	0.94	0.97	0.97	0.98	0.98	0.02	0.01	0.01	0.00	0.00	0.00	0.00
Mauritania	0.85	0.90	0.94	0.96	0.97	0.98	0.98	0.02	0.01	0.01	0.01	0.01	0.00	0.00
Northern Africa – Sahara (mean and st. dev.)	**0.88**	**0.92**	**0.94**	**0.97**	**0.97**	**0.98**	**0.98**	**0.03**	**0.02**	**0.02**	**0.01**	**0.01**	**0.01**	**0.01**
Niger	0.72	0.85	0.89	0.91	0.92	0.94	0.95	0.09	0.09	0.07	0.05	0.05	0.03	0.02
Mali	0.75	0.85	0.89	0.93	0.95	0.96	0.96	0.04	0.03	0.02	0.02	0.02	0.01	0.01
Bodélé	0.96	0.98	0.98	0.99	0.99	0.99	0.99	0.04	0.02	0.02	0.01	0.01	0.01	0.01
Sahel (mean and st. dev.)	**0.81**	**0.89**	**0.92**	**0.94**	**0.95**	**0.96**	**0.97**	**0.13**	**0.07**	**0.05**	**0.04**	**0.04**	**0.03**	**0.02**
Ethiopia	0.80	0.86	0.90	0.92	0.94	0.97	0.97	0.03	0.03	0.02	0.02	0.01	0.01	0.01
Saudi Arabia	0.88	0.93	0.96	0.98	0.98	0.98	0.98	0.03	0.02	0.01	0.01	0.01	0.00	0.00
Kuwait	0.95	0.97	0.98	0.98	0.99	0.99	0.99	0.02	0.01	0.01	0.01	0.01	0.01	0.00
Eastern Africa and the Middle East (mean and st. dev.)	**0.88**	**0.92**	**0.94**	**0.96**	**0.97**	**0.98**	**0.98**	**0.07**	**0.05**	**0.04**	**0.03**	**0.03**	**0.01**	**0.01**
Gobi	0.88	0.92	0.94	0.96	0.97	0.97	0.97	0.04	0.03	0.02	0.01	0.01	0.01	0.01
Taklimakan	0.82	0.88	0.92	0.95	0.96	0.96	0.96	0.03	0.02	0.02	0.01	0.01	0.01	0.01
Eastern Asia (mean and st. dev.)	**0.85**	**0.90**	**0.93**	**0.96**	**0.96**	**0.97**	**0.97**	**0.04**	**0.03**	**0.02**	**0.01**	**0.01**	**0.01**	**0.01**
Arizona	0.93	0.96	0.97	0.98	0.98	0.99	0.99	0.01	0.01	0.01	0.00	0.00	0.00	0.00
North America (mean and st. dev.)	**0.93**	**0.96**	**0.97**	**0.98**	**0.98**	**0.99**	**0.99**	**0.01**	**0.01**	**0.01**	**0.00**	**0.00**	**0.00**	**0.00**
Atacama	0.89	0.93	0.94	0.97	0.97	0.98	0.98	0.03	0.02	0.02	0.01	0.01	0.01	0.01
Patagonia	0.88	0.91	0.94	0.96	0.97	0.98	0.98	0.02	0.02	0.01	0.01	0.01	0.00	0.01
South America (mean and st. dev.)	**0.89**	**0.92**	**0.94**	**0.96**	**0.97**	**0.98**	**0.98**	**0.00**	**0.01**	**0.00**	**0.00**	**0.00**	**0.00**	**0.00**
Namib-1	0.91	0.95	0.96	0.98	0.98	0.99	0.99	0.02	0.01	0.01	0.00	0.00	0.00	0.00
Namib-2	0.74	0.82	0.86	0.92	0.94	0.96	0.97	0.03	0.02	0.02	0.01	0.01	0.01	0.01
Southern Africa (mean and st. dev.)	**0.83**	**0.88**	**0.91**	**0.95**	**0.96**	**0.98**	**0.98**	**0.12**	**0.09**	**0.07**	**0.04**	**0.03**	**0.02**	**0.02**
Australia	0.70	0.81	0.85	0.91	0.93	0.96	0.97	0.04	0.03	0.02	0.01	0.01	0.01	0.01
Australia (mean and st. dev.)	**0.70**	**0.81**	**0.85**	**0.91**	**0.93**	**0.96**	**0.97**	**0.04**	**0.03**	**0.02**	**0.01**	**0.01**	**0.01**	**0.01**
Full dataset (mean and st. dev.)	**0.85**	**0.91**	**0.93**	**0.96**	**0.96**	**0.97**	**0.98**	**0.08**	**0.05**	**0.04**	**0.03**	**0.02**	**0.01**	**0.01**
Full dataset median	**0.88**	**0.92**	**0.94**	**0.96**	**0.97**	**0.98**	**0.98**							

Full da­taset 10% percentile	0.74	0.84	0.88	0.92	0.94	0.96	0.96						
Full da­taset 90% percentile	0.93	0.96	0.97	0.98	0.99	0.99	0.99						

1130

Table 6. Results of the linear fit between k and SSA and the mass concentration of iron oxides, $MC_{Fe-ox\%}$, hematite, $MC_{Hem\%}$, goethite, $MC_{Goeth\%}$, and elemental iron, $MC_{Fe\%}$ in dust. Column 1 indicates the wavelength; ($a ± σa$) indicates the retrieved slope and its estimated uncertainty; ($b ± σb$) indicates the retrieved intercept and its estimated uncertainty; R^2 denotes the correlation coefficient and $χ^2_{red}$ is the reduced chi–square of the fit.

	$k = a\,MC_{Fe\text{-}ox\,\%} + b$			$SSA = a\,MC_{Fe\text{-}ox\,\%} + b$		
Wavelength (nm)	$a ± σa$	$b ± σb$	R^2 ; $χ^2_{red}$	$a ± σa$	$b ± σb$	R^2 ; $χ^2_{red}$
370	$(11.9 ± 2.4)\,10^{-4}$	$(2.4 ± 4.6)\,10^{-4}$	0.88 ; 0.6	$(-5.8 ± 0.8)\,10^{-2}$	$(1.00 ± 0.02)$	0.83 ; 1.7
470	$(9.0 ± 1.7)\,10^{-4}$	$(1.7 ± 3.2)\,10^{-4}$	0.89 ; 0.8	$(-3.8 ± 0.6)\,10^{-2}$	$(1.00 ± 0.01)$	0.78 ; 1.8
520	$(6.8 ± 1.3)\,10^{-4}$	$(1.3 ± 2.4)\,10^{-4}$	0.90 ; 0.9	$(-2.9 ± 0.4)\,10^{-2}$	$(1.01 ± 0.01)$	0.76 ; 2.0
590	$(4.5 ± 0.9)\,10^{-4}$	$(0.9 ± 1.6)\,10^{-4}$	0.85 ; 1.4	$(-1.8 ± 0.3)\,10^{-2}$	$(1.00 ± 0.01)$	0.75 ; 2.3
660	$(4.3 ± 0.8)\,10^{-4}$	$(0.8 ± 1.4)\,10^{-4}$	0.81 ; 1.6	$(-1.3 ± 0.2)\,10^{-2}$	$(1.00 ± 0.00)$	0.75 ; 2.2
880	$(3.4 ± 0.6)\,10^{-4}$	$(0.6 ± 1.2)\,10^{-4}$	0.79 ; 1.0	$(-0.76 ± 0.16)\,10^{-2}$	$(1.00 ± 0.00)$	0.79 ; 1.4
950	$(3.2 ± 0.6)\,10^{-4}$	$(0.6 ± 1.0)\,10^{-4}$	0.77 ; 1.1	$(-0.62 ± 0.13)\,10^{-2}$	$(0.99 ± 0.00)$	0.78 ; 1.1
	$k = a\,MC_{Hem\,\%} + b$			$SSA = a\,MC_{Hem\,\%} + b$		
Wavelength (nm)	$a ± σa$	$b ± σb$	R^2 ; $χ^2_{red}$	$a ± σa$	$b ± σb$	R^2 ; $χ^2_{red}$
370	$(9.7 ± 2.7)\,10^{-4}$	$(2.7 ± 4.0)\,10^{-4}$	0.67 ; 1.9	$(-4.4 ± 0.6)\,10^{-2}$	$(0.95 ± 0.01)$	0.73 ; 3.5
470	$(8.3 ± 1.9)\,10^{-4}$	$(1.9 ± 2.7)\,10^{-4}$	0.72 ; 1.9	$(-3.0 ± 0.4)\,10^{-2}$	$(0.97 ± 0.01)$	0.76 ; 3.2
520	$(6.9 ± 1.5)\,10^{-4}$	$(1.5 ± 2.0)\,10^{-4}$	0.74 ; 2.0	$(-2.2 ± 0.3)\,10^{-2}$	$(0.98 ± 0.00)$	0.78 ; 3.3
590	$(3.7 ± 0.8)\,10^{-4}$	$(0.9 ± 1.2)\,10^{-4}$	0.61 ; 2.1	$(-1.3 ± 0.2)\,10^{-2}$	$(0.99 ± 0.00)$	0.71 ; 2.7
660	$(3.7 ± 0.8)\,10^{-4}$	$(0.8 ± 1.1)\,10^{-4}$	0.51 ; 2.6	$(-0.9 ± 0.2)\,10^{-2}$	$(0.99 ± 0.00)$	0.62 ; 2.5
880	$(2.9 ± 0.7)\,10^{-4}$	$(0.7 ± 1.1)\,10^{-4}$	0.43 ; 2.1	$(-0.6 ± 0.1)\,10^{-2}$	$(0.99 ± 0.00)$	0.57 ; 1.8
950	$(2.6 ± 0.6)\,10^{-4}$	$(0.6 ± 0.9)\,10^{-4}$	0.46 ; 2.1	$(-0.5 ± 0.1)\,10^{-2}$	$(0.99 ± 0.00)$	0.49 ; 1.7
	$k = a\,MC_{Goeth\,\%} + b$			$SSA = a\,MC_{Goeth\,\%} + b$		
Wavelength (nm)	$a ± σa$	$b ± σb$	R^2 ; $χ^2_{red}$	$a ± σa$	$b ± σb$	R^2 ; $χ^2_{red}$
370	$(9.0 ± 2.5)\,10^{-4}$	$(2.5 ± 2.2)\,10^{-4}$	0.47 ; 1.8	$(-13.4 ± 6.9)\,10^{-3}$	$(0.90 ± 0.01)$	0.32 ; 6.8
470	$(5.5 ± 1.7)\,10^{-4}$	$(1.7 ± 1.5)\,10^{-4}$	0.43 ; 2.3	$(-8.3 ± 4.7)\,10^{-3}$	$(0.94 ± 0.00)$	0.21 ; 6.2
520	$(3.4 ± 1.1)\,10^{-4}$	$(1.1 ± 1.2)\,10^{-4}$	0.41 ; 2.5	$(-4.9 ± 3.2)\,10^{-3}$	$(0.96 ± 0.00)$	0.17 ; 6.4
590	$(0.5 ± 0.6)\,10^{-4}$	$(0.6 ± 0.8)\,10^{-4}$	0.50 ; 3.2	$(0.9 ± 2.0)\,10^{-3}$	$(0.97 ± 0.00)$	0.23 ; 5.5
660	$(2.2 ± 0.8)\,10^{-4}$	$(0.8 ± 0.7)\,10^{-4}$	0.55 ; 3.6	$(0.2 ± 1.6)\,10^{-3}$	$(0.98 ± 0.00)$	0.34 ; 4.4
880	$(2.6 ± 0.8)\,10^{-4}$	$(0.8 ± 0.6)\,10^{-4}$	0.62 ; 2.4	$(-1.1 ± 1.4)\,10^{-3}$	$(0.98 ± 0.00)$	0.47 ; 3.0
950	$(2.6 ± 0.8)\,10^{-4}$	$(0.8 ± 0.6)\,10^{-4}$	0.55 ; 2.5	$(-2.1 ± 1.4)\,10^{-3}$	$(0.98 ± 0.00)$	0.54 ; 2.6
	$k = a\,MC_{Fe\,\%} + b$			$SSA = a\,MC_{Fe\,\%} + b$		
Wavelength (nm)	$a ± σa$	$b ± σb$	R^2 ; $χ^2_{red}$	$a ± σa$	$b ± σb$	R^2 ; $χ^2_{red}$
370	$(6.0 ± 1.4)\,10^{-4}$	$(1.4 ± 0.7)\,10^{-4}$	0.60 ; 1.5	$(-2.7 ± 0.4)\,10^{-2}$	$(1.02 ± 0.02)$	0.67 ; 3.1
470	$(4.7 ± 1.0)\,10^{-4}$	$(1.0 ± 0.5)\,10^{-4}$	0.62 ; 1.7	$(-1.8 ± 0.3)\,10^{-2}$	$(1.02 ± 0.01)$	0.72 ; 2.8
520	$(3.9 ± 0.8)\,10^{-4}$	$(0.8 ± 3.9)\,10^{-4}$	0.65 ; 1.6	$(-1.3 ± 0.2)\,10^{-2}$	$(1.01 ± 0.01)$	0.72 ; 2.9
590	$(2.5 ± 0.5)\,10^{-4}$	$(0.5 ± 2.4)\,10^{-4}$	0.56 ; 1.7	$(-0.8 ± 0.1)\,10^{-2}$	$(1.01 ± 0.01)$	0.70 ; 2.4
660	$(2.0 ± 0.4)\,10^{-4}$	$(0.4 ± 1.7)\,10^{-4}$	0.48 ; 1.9	$(-0.5 ± 0.1)\,10^{-2}$	$(1.00 ± 0.00)$	0.62 ; 2.0
880	$(1.8 ± 0.4)\,10^{-4}$	$(0.4 ± 2.0)\,10^{-4}$	0.40 ; 1.8	$(-0.4 ± 0.1)\,10^{-2}$	$(1.00 ± 0.00)$	0.54 ; 1.6
950	$(1.4 ± 0.3)\,10^{-4}$	$(0.3 ± 1.4)\,10^{-4}$	0.45 ; 2.0	$(-0.3 ± 0.1)\,10^{-2}$	$(1.00 ± 0.00)$	0.49 ; 1.5

Figure 1. Flowchart illustrating the procedure for data treatment and retrieval of physical and chemical (size, composition) and spectral optical properties (single scattering albedo, SSA, and complex refractive index) of mineral dust aerosols.
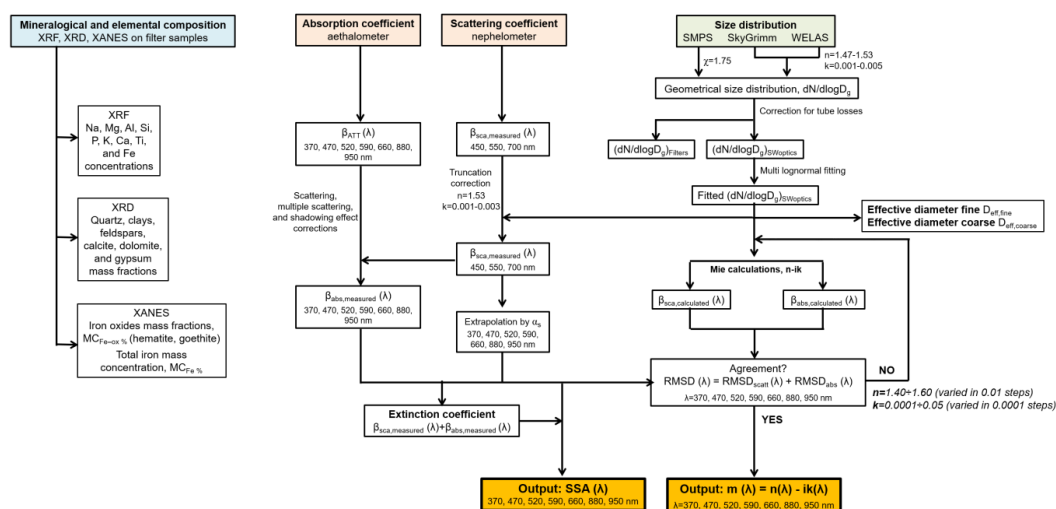
Figure 2. Box and whisker plot showing the full variability of hematite and goethite mass fractions in the clay and silt soil fractions in the dust source regions at the global scale by considering desert source areas as reported in Ginoux et al. (2012) and DB17. Data are from the soil mineralogical database by Journet et al. (2014). Dots indicate hematite and goethite soil content (extracted from Journet et al.) for the nineteen soils used in the CESAM experiments. The Journet database assumes that the iron oxides in the silt fraction consist only of goethite.
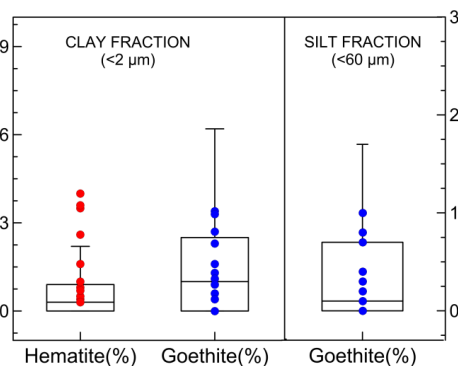
Figure 3. Top panel: time series of the aerosol mass concentration (cross symbols) and effective fine ($D_{eff,fine}$, open dots) and coarse diameter ($D_{eff,coarse}$, open squares) measured inside the CESAM chamber (red symbols) and at the input of the SW instruments (black symbols) for one experiment (Morocco dust). Bottom panel: time series of the scattering β_{sca} and absorption β_{abs} coefficients at 370 nm for the same experiment. Mass concentrations are reported as 6-sec data, while all other quantities are 10–min averages.
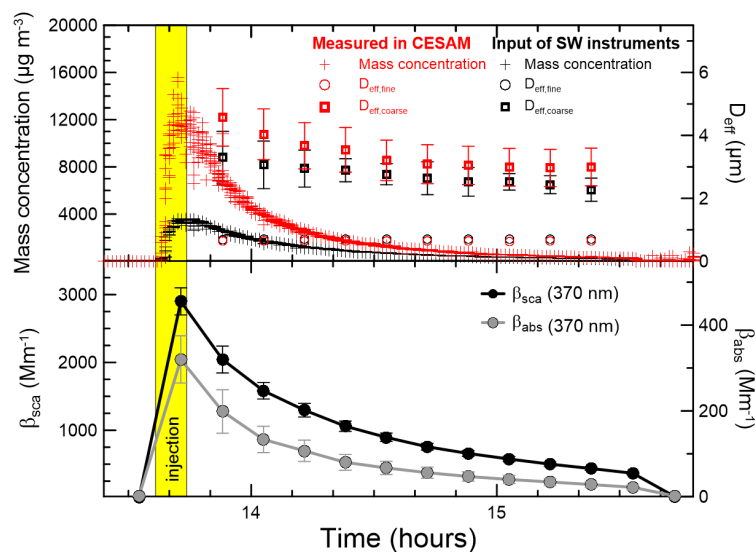
1188   **Figure 4.** Comparison of dust size distributions sensed by the SW optical instruments (behind the SW

1189   instruments inlet $(dV/dlogD_g)_{SWoptics}$), with field data for long–range transported dust. The thick black line

1190   represents the mean value of $(dV/dlogD_g)_{SWoptics}$ at the peak of the dust injection in CESAM for experi-

1191   ments with the different samples. The grey shaded area indicates the range of $(dV/dlogD_g)_{SWoptics}$ for all

1192   samples. The dotted black line shows the average of the dust size distribution at the peak of the injection

1193   inside the CESAM chamber from DB17. Field data are from: Formenti et al. (2001) (CLAIRE campaign

1194   in Suriname, South America), Maring et al. (2003) and Denjean et al. (2016b) (PRIDE and DUST-AT-

1195   TACK campaigns in Puerto Rico, Caraibes), Müller et al. (2011) and Chen et al. (2011) (SAMUM2 and

1196   NAMMA campaigns in Cape Verde, eastern Atlantic). For comparison, data taken close to the source

1197   in Niger from Formenti et al. (2011) during the AMMA campaign are also shown. All data are reported

1198   as volume size distributions normalised at the maximum.

1199

1200
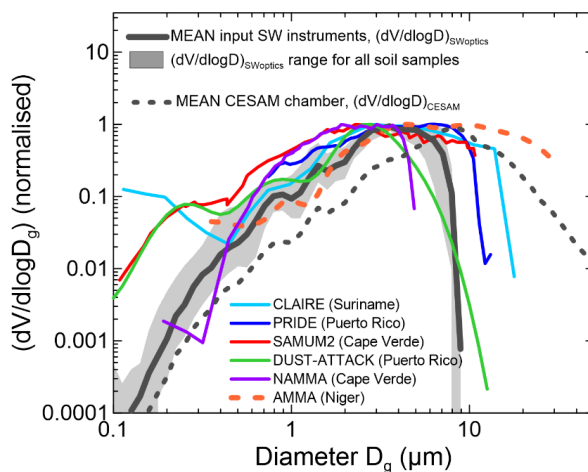
1201
1202
1203
1204
1205
1206
1207
1208
1209
1210
1211
1212
1213
1214
1215

1216 **Figure 5.** Spectral extinction coefficient, absorption coefficient, SSA, and real (n) and imaginary (k)

1217 parts of the refractive index at the peak of the dust injection in the chamber and after 30 and 90 minutes

1218 for Morocco and Algeria dust samples. Data are reported at the seven aethalometer wavelengths (370,

1219 470, 520, 590, 660, 880, and 950 nm) as 10–min averages. In the top panel we report the extinction

1220 calculated as the sum of scattering and absorption coefficients. For the sake of clarity error bars are not

1221 shown for SSA, n, and k data.

1222
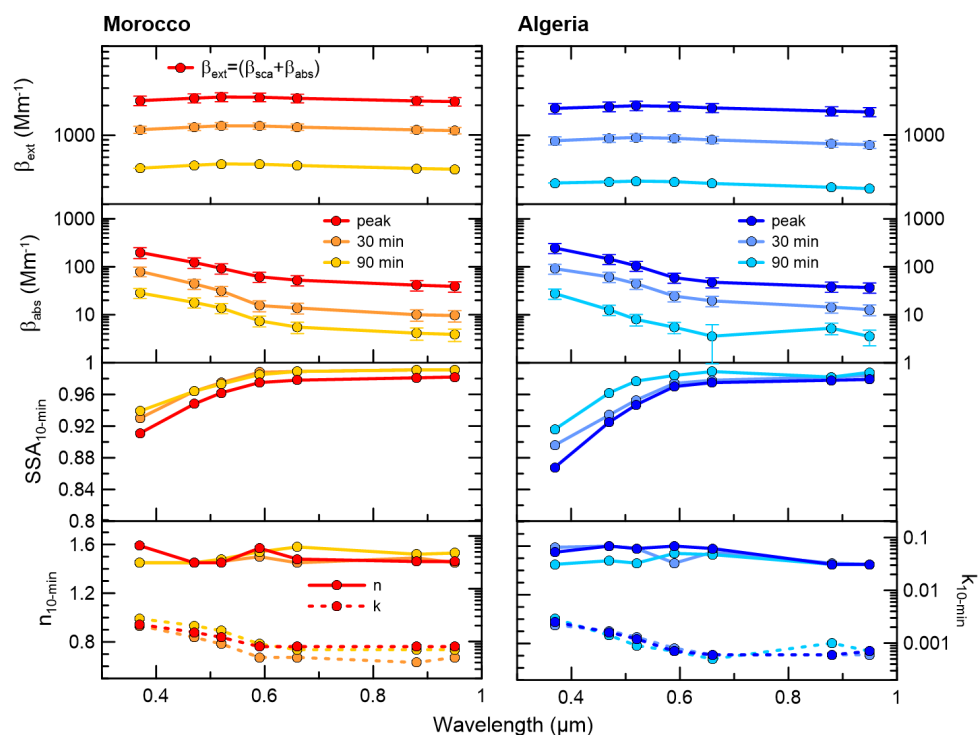
1223
1224
1225
1226
1227
1228
1229
1230
1231
1232
1233
1234
1235

Figure 6. (a) Real (n) and imaginary (k) parts of the dust complex refractive index and (b) single scattering albedo (SSA$_{AVG}$) at seven wavelengths between 370 and 950 nm obtained for the 19 aerosol samples analyzed in this study. Data for the refractive index correspond to the time average of the 10 min values obtained between the peak of the injection and 120 min later. The error bar corresponds to the absolute uncertainty in n and k, estimated to be <8% for n and between 13 and 75 % for k. SSA$_{AVG}$ data correspond to the fit of the 10 min values of β_{sca} versus β_{abs}, and the uncertainty is between 1% and 12% at 370 nm and between 1% and 3% at 950 nm.

a)

b)
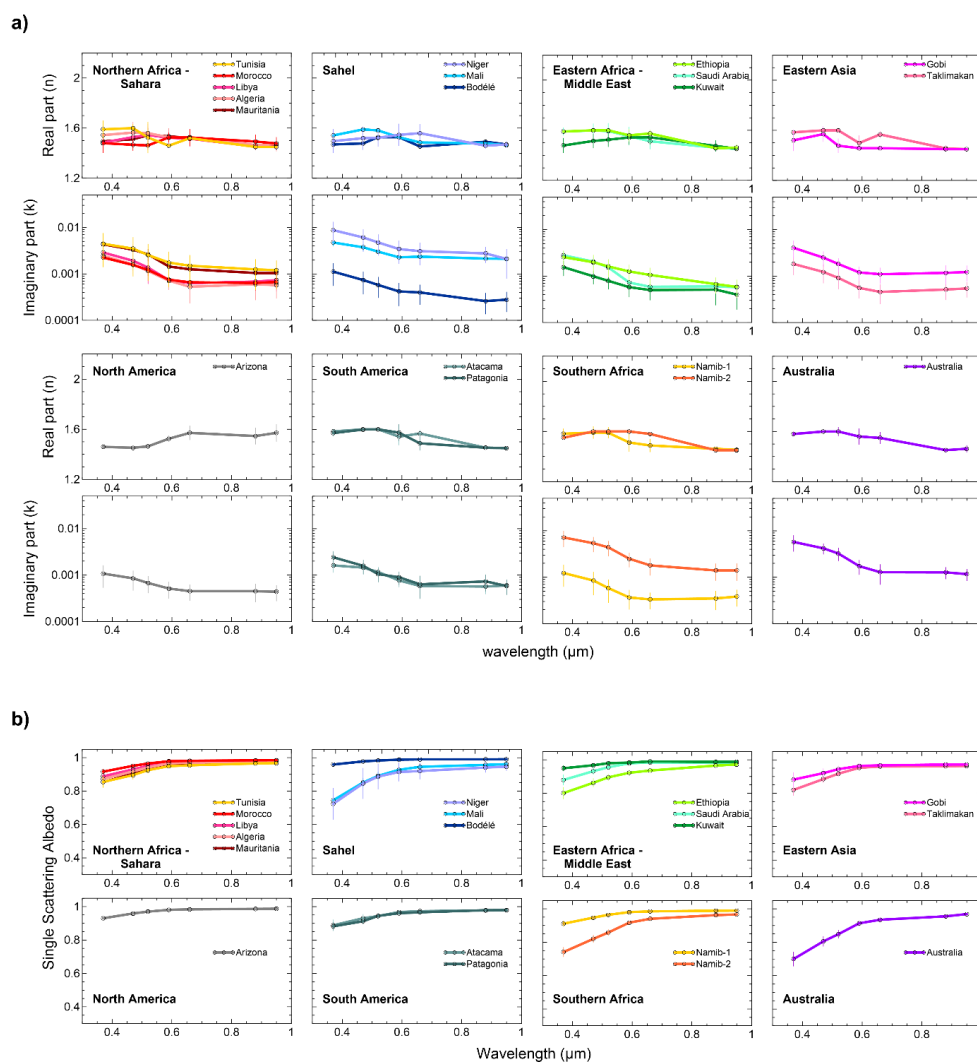
Figure 7. Comparison of results obtained in this study (a) with literature–compiled values (b) of the dust real and imaginary parts of the refractive index (n, k) and single scattering albedo (SSA) in the SW spectral range. The regions in gray in panel a) indicate the full range of variability obtained in this study, and the gray thick lines are the means of k and SSA obtained for the different aerosol samples. Literature values in panel b) include estimates from ground-based and aircraft observations during field campaigns, laboratory studies, AERONET inversions, and estimates from dust mineralogical composition. Data are in some cases for the full dust size distribution, while in other only the fine fraction below about 2 µm is measured (identified with *).

The main provenance of the dust and datasets from the literature is provided in the following: Volz et al. (1972) is data for rainout dust collected in Germany; Patterson et al. (1977) is Saharan dust; Hess et al. (1998) is data from the OPAC database; Colarco et al. (2002) is data for dust from Dakar, Sal, and Tenerife; Dubovik et al. (2002) included data from Bahrain-Persian Gulf and Solar Village-Saudi Arabia AERONET stations; Haywood et al. (2003) is dust from Mauritania; Sinyuk et al. (2003) is data from Cape Verde, Dakar, and Burkina Faso; Clarke et al. (2004) is Asian dust offshore of China, Japan, and Korea; Linke et al. (2006)-A is dust from Cairo; Linke et al. (2006)-B is dust from Morocco; Balkanski et al (2007) is calculated from mineralogical composition assuming a 1.5% hematite mass fraction in dust; Todd et al. (2007) is from Bodélé; Osborne et al. (2008) is from Niger; Otto et al. (2009), Petzold et al. (2009), Schladitz et al. (2009), and Muller et al. (2010, 2011) is dust originated mostly in Morocco; McConnell et al. (2008, 2010) is dust from Niger/Senegal; Chen et al. (2011) is dust from Western Sahara; Formenti et al. (2011) in the k plot is an average of airborne observations for the AMMA campaign in Niger, while for the SSA plot, Formenti et al. (2011)-A is from observations in the Saharan Air Layer, -B is from Bodélé/Sudan, and –C is a Sahelian uplift episode; Johnson et al. (2011) is dust from Western Sahara; Moosmüller et al. (2012) analysed samples from Middle East, Mali and Spain, and here we report the average of their obtained values; Wagner et al. (2012) obtained k values for several samples from Cairo and Burkina Fasu and here we report and average of its results; Ryder et al. (2013) is dust from Western Sahara and Mauritania and we report in both k and SSA plots the average of their observations; Engelbrecht et al. (2016) analysed many dust samples from all over the world, here we report their measured minimum and maximum of the dust SSA that are –A from California and –B from the Etosha Pan in Namibia; Steigmann and Yang (2017) modelled the refractive index of dust based on assumed mineralogical compositions typical for Northern and Southern Sahara and Western and Eastern Asia dust, and here we report the average of their results for both n and k. Uncertainties in the field observations have been omitted for the sake of clarity. The legend identifies the line styles used in the plots.

(The different acronyms spell out as: AERONET = Aerosol Robotic Network; OPAC = Optical Properties of Aerosols and Clouds; SHADE = Saharan Dust Experiment; BODEX = The Bodélé Dust Experiment; DABEX = Dust and Biomass Experiment; SAMUM = Saharan Mineral Dust Experiment; DODO = Dust Outflow and Deposition to the Ocean; AMMA = African Monsoon Multidisciplinary Analysis; NAMMA = NASA African Monsoon Multidisciplinary Analysis; ACE-Asia = Asian Pacific Regional Aerosol Characterization Experiment; GERBILS = Geostationary Earth Radiation Budget Intercomparison of Longwave and Shortwave radiation).
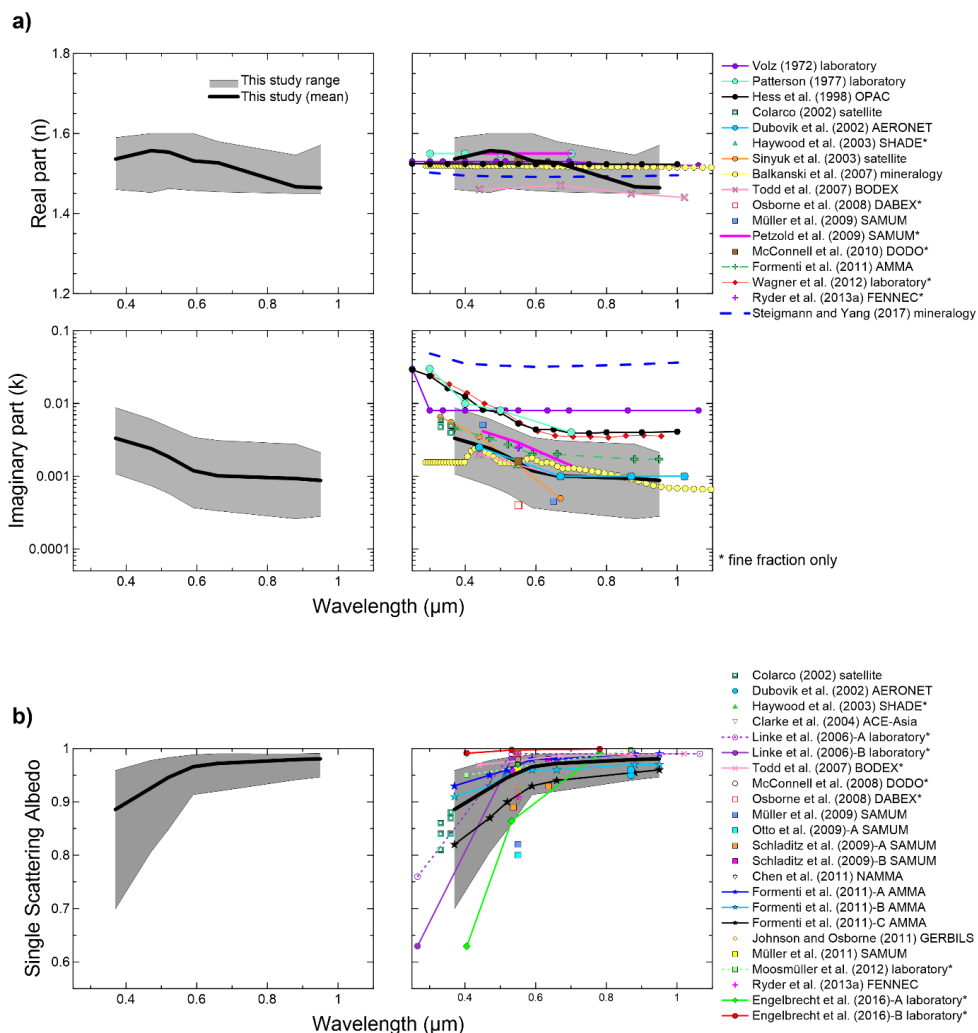
1289
1290
1291
1292
1293
1294
1295
1296
1297
1298
1299
1300
1301

Figure 8. Experiment–averaged imaginary part of the refractive index (k, top panels) and single scattering albedo (SSA, bottom panels) at 370, 520, and 950 nm versus the mass concentration of iron oxides ($MC_{Fe-ox\%}$), hematite ($MC_{Hem\%}$), goethite ($MC_{Goeth\%}$), and elemental iron ($MC_{Fe\%}$) measured for the different dust samples analysed in this study. The calculated linear fit regression lines are shown, together with the correlation coefficients of the fits (R^2). The legend indicates the line styles used in the plots. Data for the Taklimakan sample were excluded from the k and SSA plots versus $MC_{Fe-ox\%}$, $MC_{Hem\%}$, and $MC_{Goeth\%}$ due to the absence of data for this sample.
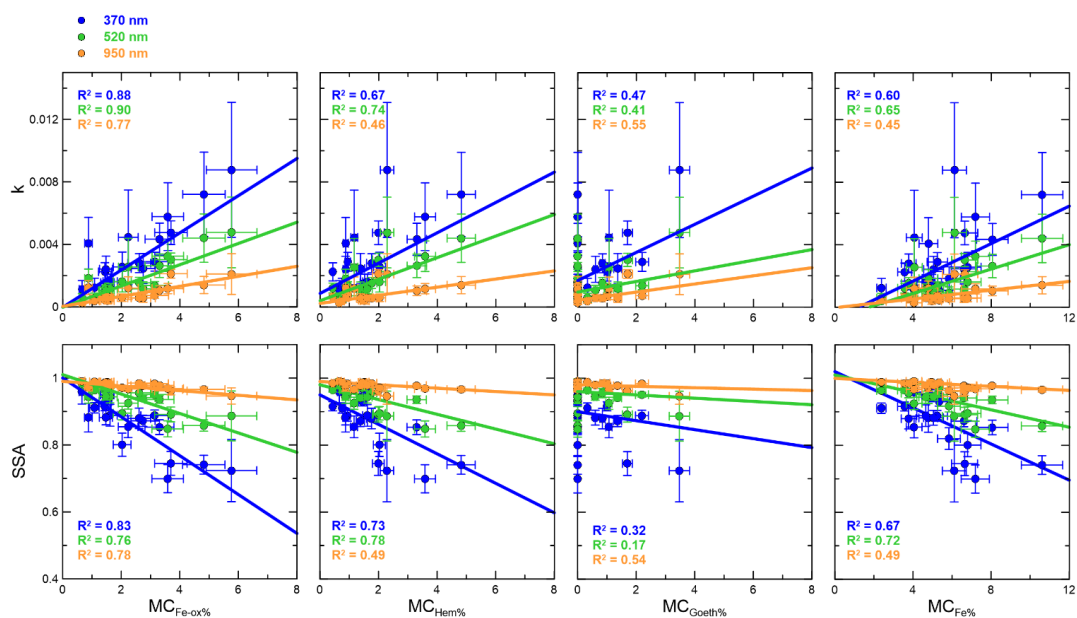
Figure 9. 10–min averaged imaginary refractive index (k_{10-min}, top panels) and single scattering albedo (SSA$_{10-min}$, bottom panels) at 370, 520, and 950 nm versus effective coarse diameter ($D_{eff,coarse}$) estimated at the input of the SW instruments. Data were classified in three classes based on the iron oxide content of the dust samples. The linear fit curves and the correlation coefficients for the linear regression fits for each dataset are also reported. The legend identifies the line styles used in the plots.